مجلة المختار للبحوث الهندسية

Al-Mukhtar Journal of Engineering Research

Volume
Issue
2023

Published by OMU

Al-Mukhtar Journal of Engineering Research

Peer-reviewed scientific journal, Volume Eight , Issue One, 2024

Published by Omar Al-Mukhtar University, Al-Bayda, Libya

Al-Mukhtar Journal of Engineering Research

5NL – LDN 281-201

A peer-reviewed journal published by Omar Al-Mukhtar University, Al Bayda, Libya
Peer-reviewed scientific journal, Volume Eight , Issue One, 2024
Email: omu.j.eng@omu.edu.ly
To pour. Box 919 Al Bayda - Libya

Al-Mukhtar Journal of Engineering Research 07: (1), 2023

Al-Mukhtar Journal of Engineering Research 07 (1): 01-11, 2023
Doi: https://doi.org/10.54172/3tm3e547

Research Article **Open Access**

High-Density Polyethylene/Kaolin Clay Composites: Optimiztion of The Injection Moulding Process Parameters Towards Minimum Shrinkage and Warpage

Abd Alraouf Treesh[(1)], Wael Elhrari[(1)] and Hussein Etmimi[(3)]

***Corresponding author:** tresh305@gmail.com, Libyan Polymer Research Center

Second Author: waelelhrari@gmail.com Libyan Polymer Research Center.

Third Author: hmetmimi@gmail.com, Libyan Polymer Research Center.

Received:
24 January 2023

Accepted:
22 November 2023

Publish online:
31 December 2023

Abstract

Optimization of the injection moulding process parameters of thermoplastic composites made of high-density polyethylene (HDPE) and kaolin clay (KC) was carried out using the Taguchi method. The parameters that were taken into consideration were melting temperature, packing pressure and packing time. Composites containing 98 wt% of HDPE and 2wt% of KC with various particle sizes of <75, 75-106 and 106-150 µm were used. Two defects that are usually associated with the injection moulding process of polymers were selected, namely shrinkage and warpage. Results showed that the optimal parameters needed to obtain a minimum shrinkage value for composites containing clay (regardless of its particle size) are very similar to those for the pure HDPE. Contrary, the optimal parameters needed to obtain a minimum warpage value depends on the size of clay particles added, which were also different from those of the pure HDPE. Results also revealed that the most effective parameter (both shrinkage and warpage) for pure HDPE and its composites with clay was the melting temperature.

Keywords: Clay, High Density Polyethylene, Injection Moulding, Shrinkage and Warpage

INTRODUCTION

Clay particles are highly recognized as fillers and are extensively utilized in polymer composites owing to their exceptional properties. [1-3]. These properties include cation exchange capabilities, swelling behaviour, plastic behaviour when wet, ability to harden when dried or fired and low permeability. Composite materials obtained from the combination of polymers and clays possess a unique set of properties that make them highly desirable for various industrial applications. These materials offer enhanced stiffness, improved strength, high impact resistance, and thermal stability, making them ideal for use in automobiles, electrically conductive materials, and other applications where such properties are needed. [4] The injection moulding process is widely used in the manufacturing of industrial parts made from polymers and polymer composites. This process involves injecting melted polymeric materials into a mould to create the desired shape. This process depends on a variety of variables, such as melting temperature, injection pressure, filling time. Although the process is considered to be very stable, however, due to some internal interactions of several parameters, the resultant product's quality could be dramatically affected. Thereafter, this process re-

quires optimization, which could improve the physical and mechanical properties of the final products.

It has been shown that optimizing the injection moulding processing parameters can be performed via several techniques [5]. Nowadays, computer-aided simulations and statistical experimental approaches can be used to achieve the required factors to obtain optimal processing conditions. Taguchi method is one of the leading statistical methods for the optimization of injection moulding processes. This method has been recently used for optimizing the processing parameters of a variety of polymers that could be injection moulded such as polyethylene [6-8], polypropylene (PP) [9, 10], recycled high-density polyethylene (HDPE) [11], acrylonitrile butadiene styrene copolymers [12], polycarbonate [13], polybutylene terephthalate [14], polyamide [15], polyurethane [16], and polystyrene [17]. Optimizing the injection moulding process of polymer composites using the Taguchi method was also under investigation. For instance, high-density polyethylene (HDPE)/TiO_2 nanocomposites were studied using this technique, where four parameters were chosen; concentration of TiO_2, barrel temperature, residence time and packing time, while mechanical properties such as yield strength, modulus of elasticity and elongation were selected as representative performance [18]. The authors found that 5wt % TiO_2, 225 ^oC barrel temperature, the residence time of 30 min and packing time of 20 seconds were found to be the optimal operating variables.

Optimization of ultrasonic injection moulding for ultra-high molecular weight polyethylene/graphite composites was also studied by the Taguchi method [19]. The authors showed that the optimal parameters to maximize the tensile strength of the composites were the mould temperature, which was the most significant parameter, followed by the graphite content. Kamaruddin et al. [20] utilized this technique to improve the quality characteristic of products made by injection moulding to reduce the shrinkage of polymer blends of PP (75%) and low density polyethylene (LDPE) (25%). Their findings showed that combination of low melting temperature, high injection pressure, low holding pressure, long holding time and long cooling time affected the shrinkage of the final product. Similarly, Mehat et al. [21] carried out a study to improve the mechanical properties of blends of recycled and virgin plastics via optimal processing parameters using the Taguchi method. Four controllable factors were chosen, which included melting temperature, injection pressure, injection time and filling time each at three levels. The results revealed that the products, which are made of 25% recycled PP and 75% virgin PP exhibited a better flexural modulus compared to the virgin PP.

Rajesg et al. [22] studied the effect of injection moulding parameters on the nanofiller dispersion of PP/clay nanocomposites. The major individual influencing parameter was the injection flow rate, which improved the nanoclay dispersion with the combination of high back pressure and high screw rotational speed. Polypropylene composites containing clay and natural fibres were also studied. Othman et al. [23-25] used polypropylene mixed with clay and fibres obtained from bamboo trees in their optimization study of processing conditions using the injection moulding method. According to them, the optimum parameters used to obtain a minimized shrinkage value were melting temperature of 170 ^oC, the pressure of 80%, and screw speed of 70% and 3 seconds of filling time. Whereas, minimum warpage was obtained when they used melting temperature of 170 ^oC, the pressure of 70%, screw speed of 70% and 2 seconds of filling time.

In a recent study carried out by our group [26], we investigated the effect of Libyan kaolin clay on the impact strength of HDPE. Our results showed that 2wt% kaolin clay added to HDPE enhanced its impact resistance up to 33% compared to virgin HDPE. Another study [27] showed the particle size of kaolin clay has a significant effect on the mechanical properties of HDPE composites. Clay

particles sizes of 75-150 µm appear to have better overall properties compared to composites containing clay particles with sizes of <75 and > 150 µm. Anova studies carried out on the same composites have shown the effect of injection temperature on shrinkage of composites with particle sizes <75 and 106-150µm was statistically significant. Also, the injection temperature has an effect on the impact strength of the composites with particle sizes <75 and 106-150µm was clear. [28] In this study, the attempt to investigate the optimization of the injection moulding process parameters of these composites was carried out. Taguchi method was used to help evaluate the best injection moulding parameters that produced the minimum shrinkage and warpage using clay with different particle sizes. Three factors, melting temperature, packing pressure and packing time and their effect on shrinkage and warpage was investigated using the Taguchi method.

EXPERIMENTAL

Materials

HDPE was used as received as the matrix polymer (SABIC Saudi Arabia, HDPE F00952, melt flow index 0.05 g/10 min and density 952 g/cm^3). Kaolin clay was supplied by Industrial Research Center in Tripoli-Libya (collected from Sabha city in Libya). It was sieved to remove impurities and then passed through different sieve sizes to get particle sizes of (<75, 75-106 and 106-150 µm).

Composite preparation

kaolin clay was dried in an air circulating oven at 85 °C for 24 hr and mixed with the polymer in (Ultra centrifugal mill ZM 200 -RETSCH) to obtain a very fine powder of the mixture. The final mixing was then carried out by melt mixing method using twin-screw extruder (Brabender, Germany) at a screw speed of 35 r.p.m. and L/D ratio of 48 at the temperature range of 160-200 °C. The temperature setup of the extruder is shown in) Table 1)The extruded composites were cooled in air and then ground. Samples for shrinkage and warpage measurements were prepared in an injection moulding machine (Xplore 12ml, Netherlands) at the various injection temperature, packing pressure and packing times.

Table (1): Temperature setup of the extruder

Zone No.	Zone 1	Zone 2	Zone 3	Zone 4	Zone 5	Zone 6
Temp (°C)	160	170	170	180	190	200

Shrinkage measurements

Shrinkage refers to the decrease in size that occurs in a linear direction when a polymeric object cools down to room temperature after being injected at molding temperature. To obtain the shrinkage value (S), three measurements are taken for each trial, and the following equation is used.

$$S = \frac{L_c - L_{ave}}{L_c}$$

Where, Lc is the actual mould cavity length (mm) and L_{ave} is the average of sample length (mm).
The actual mould cavity length (Lc) is calculated as: $Lc = L\,[1+\alpha\,(T_{mould}-T_{ambient})]$
Where, α is the coefficient of thermal expansion for steel (6.45×10^{-6} 1/°F), L is the measured cavity length (mm), T_{mould} is the mould temperature in °F, and $T_{ambient}$ is ambient temperature in °F.

Warpage measurements

The thickness of the sample was measured at three different places by using a digital micrometre. Three measurements for each trial were taken, and the average warpage value was used. The warpage (Z) was calculated using the following formula:

$Z = h - t_a$

Where, h is the depth of the mould cavity (mm) and t_a is the average of sample thickness (mm).

Design of Experiment

Taguchi method with $L_9 3^3$ orthogonal array using the statistical software Minilab-19 was adopted and used in this study. The injection moulding parameters were investigated are melting temperature, packing pressure and packing time. These factors were set at three levels for three different composites containing different clay particle sizes (<75, 75-106 and 106-150 µm) as shown in) Table 2). In this study, the smaller value of shrinkage and warpage should give a better quality characteristic of the final product. Therefore, the "smaller is better" options as signal to noise ratio (S/N) was used. (Table 3) shows the details of the orthogonal array used for the Taguchi study.

Table (2): Injection moulding parameters, factor symbols and their level selection.

Parameters	Unites	Factor symbol	Level 1	Level 2	Level 3
Injection temperature (NT)	(^{o}C)	A	180	200	220
Packing pressure (PP)	(Bar)	B	6	8	10
Packing time (PT)	(Sec)	C	1	2	3

Table (3): Taguchi method $L_9 3^3$ orthogonal array

Trial No	A (NT)	B (PP)	C (PT)
1	1 (180)	1 (6)	1 (1)
2	1 (180)	2 (8)	2 (2)
3	1 (180)	3 (10)	3 (3)
4	2 (200)	1 (6)	2 (2)
5	2 (200)	2 (8)	3 (3)
6	2 (200)	3 (10)	1 (1)
7	3 (220)	1 (6)	3 (3)
8	3 (220)	2 (8)	1 (1)
9	3 (220)	3 (10)	2 (2)

RESULT AND DISSECTION

The focus of the study was to investigate the effect of injection moulding process parameters on some defects of parts made from HDPE/kaolin clay composites namely shrinkage and warpage. The Taguchi approach was utilized to optimize the injection process of such composites towards a minimum shrinkage and warpage. Three different clay particle sizes were used, and their effect on the optimization process was also discussed. For comparison, the optimization of pure HDPE was also studied. A confirmation test based on experimental trials was carried out. (Table 4) shows the average shrinkage and warpage values for pure HDPE and all composites (containing clay with different particle sizes) based on each trial.

Based on the results achieved in) Table 4), the value for a signal to noise (S/N) ratio was calculated and used to measure the quality characteristic of the sample. In this study, the smaller values of shrinkage and warpage shall give a better quality characteristic. Therefore, the option "smaller is better" was used. The response values of the S/N ratio for shrinkage and warpage for pure HDPE and all composites containing clay of different particle sizes of <75, 75-106 and 106-150 µm are shown in) Tables 5-8).

Table (4): The average shrinkage and warpage for different composites with different particle sizes

Trial No	Pure HDPE		75 μm particles size		106 μm particles size		150 μm particles size	
	Shrinkage	Warpage	Shrinkage	Warpage	Shrinkage	Warpage	Shrinkage	Warpage
1	0.026	0.14	0.021	0.06	0.051	0.02	0.051	0.05
2	0.009	0.14	0.014	0.04	0.042	0.04	0.041	0.04
3	0.008	0.14	0.022	0.05	0.053	0.04	0.053	0.11
4	0.025	0.14	0.032	0.06	0.061	0.07	0.063	0.05
5	0.017	0.10	0.023	0.07	0.056	0.05	0.055	0.05
6	0.041	0.10	0.032	0.04	0.067	0.07	0.063	0.07
7	0.029	0.07	0.032	0.04	0.059	0.06	0.056	0.07
8	0.035	0.14	0.032	0.04	0.070	0.06	0.063	0.06
9	0.025	0.07	0.035	0.06	0.057	0.02	0.062	0.06

Table (5): The response values of S/N ratio for shrinkage and warpage for pure HDPE

HDPE	Level	NT		PP		PT	
		Shrinkage	Warpage	Shrinkage	Warpage	Shrinkage	Warpage
---	1	37.67	17.08	31.36	19.08	29.31	18.05
---	2	31.54	18.05	34.77	18.05	34.70	19.08
---	3	30.56	20.06	33.64	20.06	35.76	20.06
Delta	--	7.11	4.01	3.41	2.01	6.44	2.01
Rank	--	1	1	3	2.5	2	2.5

Table (6): The response values of S/N ratio for shrinkage and warpage for composites containing clay particle size of <75 μm

Clay particle size (μm)	Level	NT		PP		PT	
		Shrinkage	Warpage	Shrinkage	Warpage	Shrinkage	Warpage
<75	1	34.31	26.14	30.94	25.61	30.97	26.78
<75	2	30.6	25.16	32.86	26.34	31.68	25.61
<75	3	29.39	26.78	30.51	26.14	31.65	25.69
Delta	--	4.93	1.62	2.35	0.73	0.71	1.17
Rank	--	1	1	2	3	3	2

Table (7): The response values of S/N ratio for shrinkage and warpage for composites containing clay particle size of 75-106 μm

Clay particle size (μm)	Level	NT		PP		PT	
		Shrinkage	Warpage	Shrinkage	Warpage	Shrinkage	Warpage
75-106	1	26.26	29.13	24.87	26.34	24.14	26.34
75-106	2	24.22	24.07	25.2	26.14	25.53	27.90
75-106	3	24.18	27.17	24.58	27.90	24.98	26.14
Delta	--	2.08	5.06	0.63	1.76	1.39	1.76
Rank	--	1	1	3	2.5	2	2.5

Table (8): The response values of S/N ratio for shrinkage and warpage for composites containing clay particle size of 106-150 µm

Clay particle size (µm)	Level	NT		PP		PT	
		Shrinkage	Warpage	Shrinkage	Warpage	Shrinkage	Warpage
106-150	1	26.24	24.30	24.87	24.78	24.55	24.52
106-150	2	24.35	25.05	25.57	26.14	25.22	26.14
106-150	3	24.33	23.73	24.48	22.15	25.15	22.41
Delta	--	1.91	1.32	1.09	3.99	0.67	3.73
Rank	--	1	3	2	1	3	2

Graphs of main effects plots for S/N ratio for shrinkage and warpage values for pure HDPE and various composites are shown in) Fig 1-4).

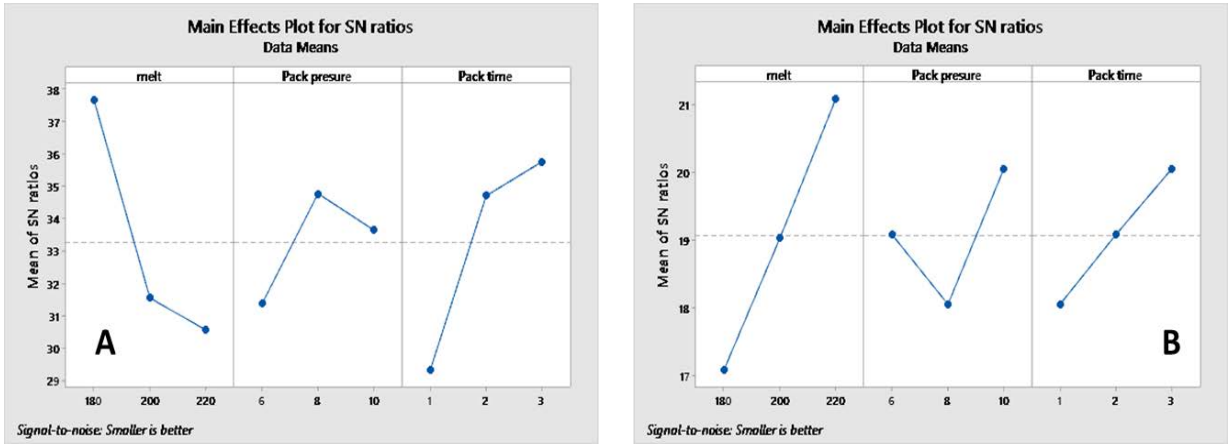

Figure (1). S/N ratio response for pure polymer a) shrinkage and b) warpage.

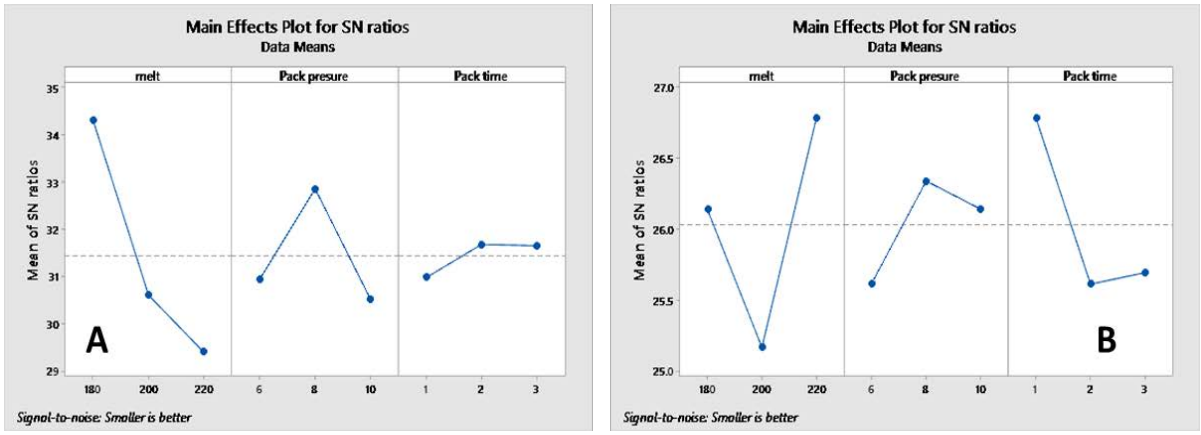

Figure (2). S/N ratio response for composite with clay particle size of <75 µm: a) shrinkage and b) warpage.

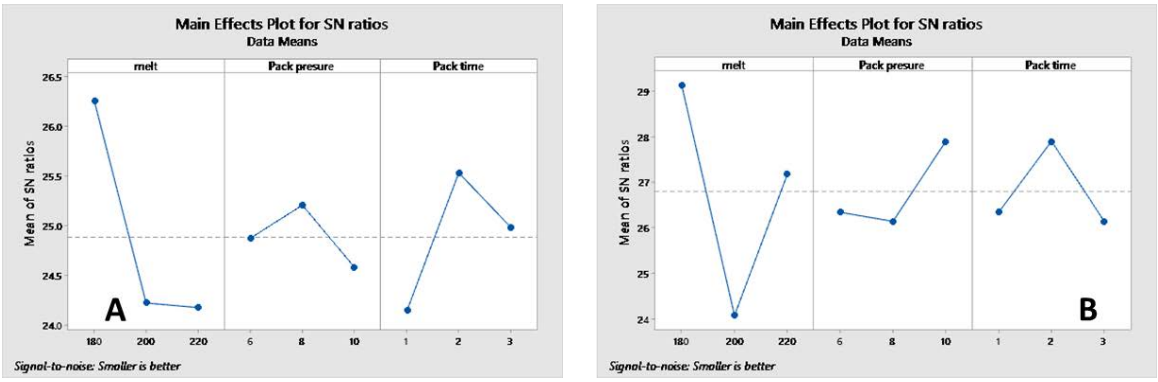

Figure (3). S/N ratio response for composite with clay particle size of 75-106 μm: a) shrinkage and b) warpage.

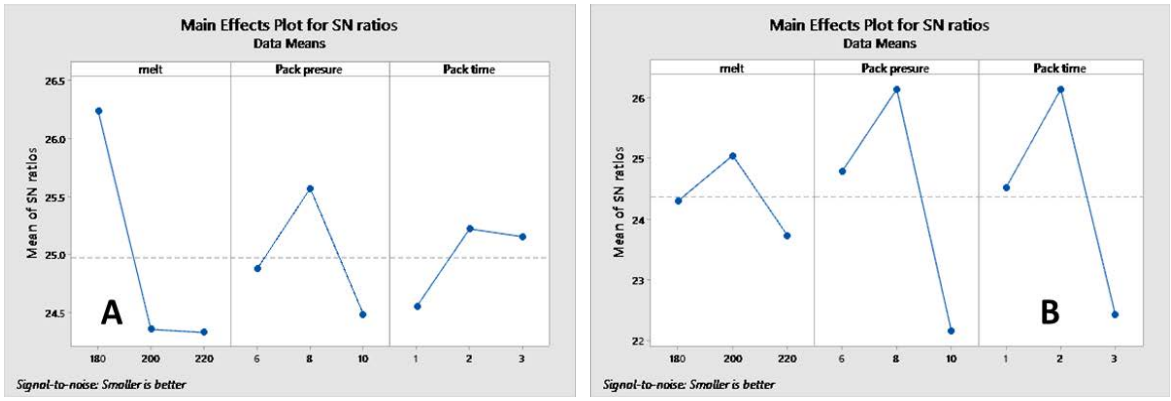

Figure (4). S/N ratio response for composite with clay particle size of 106-150 μm: a) shrinkage and b) warpage.

The best conditions can be determined by selecting the level with the highest response value for each factor. Based on these results, the best conditions that were used to obtain the least shrinkage and warpage values for pure HDPE and each composite were selected, which are summarized in (Table 9).

Table (9): The optimal combination of conditions for minimizing shrinkage and warpage

Clay particle size (μm)	**NT**		**PP**		**PT**	
	Shrinkage	Warpage	Shrinkage	Warpage	Shrinkage	Warpage
No clay	37.67	20.06	34.77	20.06	35.76	20.06
Level	1	3	2	3	3	3
<75	34.31	26.78	32.86	26.34	31.68	26.78
Level	1	3	2	2	2	1
75-106	26.26	29.13	25.2	27.9	25.53	27.9
Level	1	1	2	3	2	2
106-150	26.24	25.05	25.57	26.14	25.22	26.14
Level	1	2	2	2	2	2

As shown in (Table 9), one can see that the optimal conditions for all composites containing clay with various particle sizes are the same for shrinkage, which was at the factor levels of A1, B2, C2. This indicates that the size of clay particles has no significant effect on the injection moulding factors studied. In addition, results showed that the conditions for all composites are slightly different from those for the pure HDPE (A1, B2, and C3). On the other hand, the size of clay particles seems to have a significant effect on the warpage values. For composites with the clay particle size of <75 μm, a minimum warpage value was obtained at levels of A3, B2, C1. For composites with the clay

particle size of 75-106 µm, the best combination of factors was obtained at levels A1, B3, C2, while composites with the clay particle size of 106-150 µm, the best combination of factors were at levels A2, B2, C2. Furthermore, the optimal conditions for pure HDPE were at levels A3, B3, C3, which are different from those for the composites. These variations indicate that the size of clay particles has a significant influence on the injection moulding process parameters under study.

Confirmation test

Confirmation tests were carried out using the best combination of conditions obtained from the Taguchi study, which resulted in the minimum shrinkage and warpage values. The test was carried out for composites only at a different. (Table 10) shows the experimental shrinkage and warpage values for all composites with various clay particle sizes.

Table (10): Shrinkage and warpage values for composites containing clay with varies particle sizes.

Defect name	Clay particle size of <75 µm	Clay particle size of 75-106 µm	Clay particle size of 106-150 µm
Shrinkage	0.016	0.018	0.015
Warpage	0.020	0.050	0.040

(Table 10) clearly shows that the shrinkage and warpage values for all composites are relatively small, similar to the values obtained at the optimization levels. The results confirm that the optimal conditions found by the Taguchi study indeed produced the minimum value of shrinkage and warpage. Taguchi's results showed the lowest shrinkage value for composites with different clay particle sizes obtained was at levels A1, B2, C2 with values between 0.015-0.018. Similarly, Taguchi results showed the lowest warpage value for composite with the clay particle size of <75 at levels A3, B2, C1. For composite with the clay particle size of 75-106 µm, the lowest warpage value was obtained at levels A1, B3, C2. For composite with the clay particle size of 106-150 µm, the lowest warpage value was obtained at levels A2, B2, C2. The warpage value between obtained were 0.02-0.05 for composites with various clay particles, which were very close to the optimal values obtained above.

CONCLUSION

Taguchi method was used to study the optimal injection moulding process parameters for composites containing high-density polyethylene (HDPE) and Kaolin clay (KC). This was carried out to predicate the best possible combination of conditions in order to minimize the shrinkage and warpage of parts made from these composites. The following can be concluded from this study:

- The optimum conditions for a minimum shrinkage

The optimal combination of parameters that gave minimum shrinkage for pure HDPE is injection temperature of 180 °C, packing pressure of 8 bar and 3 sec of packing time. Those for composite containing KC with particle sizes of <75, 75-106 and 106-150 µm are injection temperature of 180 °C, packing pressure of 8 bar and 2 sec of packing time. The most effective parameter for pure HDPE and all composites containing clay particles of <75, 75-106 and 106-150 µm is injection temperature.

- The optimum conditions for a minimum warpage

The optimal combination of parameters that gave minimum warpage for pure HDPE are injection temperature of 220 °C, packing pressure of 10 bar and 3 sec of packing time Those for composite containing KC with the particle size of <75, 75-106 and 106-150 µm are injection temperature of 180 °C, packing pressure of 8 bar and 1 sec of packing time, injection temperature of 180 °C, pack-

ing pressure of 10 bar and 2 sec of packing time and injection temperature of 200 °C, packing pressure of 8 bar and 2 sec of packing time, respectively. The most effective parameter for pure HDPE and composites containing clay particles of <75 and 75-106 µm is the injection temperature, while the most effective parameter for composites containing clay particle size of 106-150 µm is the packing pressure.

REFERENCES

[1] F. Gao, Clay/polymer composites: the story, Materials today, **7** (2004) 50-55.

[2] S. Leporatti, Polymer Clay Nano-composites, Polymers, 11 (2019) 1-4.

[3] T. Pinnavaia, G. Beall, eds. Polymer-clay nanocomposites 2001 wiley.

[4] L. Hu, E. Leclair, M. Poulin, F. Colas, P. Baldet, P. Vuillaume, Clay/Polyethylene Composites with Enhanced Barrier Properties for Seed Storage, Polymers & Polymer Composites, 24 (2016) 387-394.

[5] P. Megat-Yousoff, M. Latif, M. Ramli, Optimizing Injection Molding Processing Parameters for Enhanced Mechanical Performance of Oil Palm Empty Fruit Bunch Hogh Density Polyethylene Composites, Journal of Applied Sciences, 11 (2011) 1618-1623.

[6] S. Lal, H. Vasudevan, Optimization of Injection Moulding Process Parameters in the Moulding of Low Density Polyethylene (LDPE), International Journal of Engineering Research and Development, **7** (2013) 35-39.

[7] M. Othman, S. Shamsudin, S. Hasan, The Effects of Parameter Settings on Shrinkage and Warpage in Injection Molding through Cadmould 3D-F Simulation and Taguchi Method, Applied Mechanics and Materials, 229-231 (2012) 2536-2540.

[8] H. Kale, U. Hambire, Optimization of Injection Molding Process Parameter for Reducing Shrinkage by Using High Density Polyethylene (HDPE) Material, International Journal of Science and Research, 4 (2013) 722-725.

[9] G. Singh, M. Pradhan, A. Verma, Effect of Injection Moulding Process Parameter on Tensile Strength Using Taguchi Method, International Journal of Mechanical, Aerospace, Industrial, Mechatronic and Manufacturing Engineering, 9 (2015) 1719-1724.

[10] A. Dwiwedi, S. Kumar, Practical application of Taguchi method for optimization of process parameters in Injection Molding Machine for PP material, International Research Journal of Engineering and Technology, 2 (2015) 264-268.

[11] J. Abdullaha, L. Shana, H. Ismail, Optimization of Injection Moulding Process Parameters for Recycled High Density Polyethylene (RHDPE) Using The Taguchi Method, International Journal of Mechanical And Production Engineering, 4 (2016) 76-81.

[12] Y. Amer, M. Moayyedian, Z. Hajiabolhasani, L. Moayyedian, Reducing Warpage in Injection Moulding Processes Using Taguchi Method Approach: ANOVA. in International conference Engineering and Applied Science. (2012).

[13] R. Pareek, J. Bhamniya, Optimization of Injection Moulding Process using Taguchi and ANOVA, International Journal of Scientific & Engineering Research, 4 (2013).

[14] R. Khavekar, H. Vasudevan, G. Vimal, Optimization of Injection Moulding Process Parameters for Manufacturing Plastic Components (PBT) Using Taguchi Method (TM), Materials Science Forum, 969 (2019) 775-780.

[15] N. Mehat, H. Noor, S. Kamaruddin. Optimization of multiple quality characteristics for injection moulded polyamide helical gear via integration of Taguchi method and Grey relational analysis, in 1st International Conference on Science, Engineering and Technology (ICSET) (2020) IOP Conf. Series: Materials Science and Engineering.

[16] T. Gaaz, A. Sulong, A. Kadhum, M. Nassir, A. Al-Amiery, Optimizing Injection Molding Parameters of Different Halloysites Type-Reinforced Thermoplastic Polyurethane Nanocomposites via Taguchi Complemented with ANOVA. Materials, 9 (2016) 1-19.

[17] Q. Jan, T. Habib, S. Noor, A. Muhammad, S. Azim, Q. Yaseen, Multi response optimization of injection moulding process parameters of polystyrene and polypropylene to minimize surface roughness and shrinkage's using integrated approach of S/N ratio and composite desirability function, Cogent Rngineering, **7** (2020) 1-30.

[18] H. Pervez, M. Mozumder, A. Mourad, Optimization of Injection Molding Parameters for HDPE/TiO2 Nanocomposites Fabrication with Multiple Performance Characteristics Using the Taguchi Method and Grey Relational Analysis, Materials, 9 (2016) 1-12.

[19] X. Sánchez-Sánchez, A. Elias-Zuñiga, M. Hernández-Avila, Processing of ultra-high molecular weight polyethylene/graphite composites by ultrasonic injection moulding: Taguchi optimization, Ultrasonics Sonochemistry, 44 (2018) 350-358.

[20] S. Kamaruddin, Z. Khan, S. Foong, Application of Taguchi Method in the Optimization of Injection Moulding Parameters for Manufacturing Products from Plastic Blend, International Journal of Engineering and Technology, 2 (2010) 574-580.

[21] N. Mehat, S. Kamaruddin, Optimization of mechanical properties of recycled plastic products via optimal processing parameters using the Taguchi method, Journal of Materials Processing Technology, 211 (2011) 1989-1994.

[22] J. Rajesh, J. Soulestin, M. Lacrampe, P. Krawczak, Effect of injection molding parameters on nanofillers dispersion in masterbatch based PP-clay nanocomposites, eXPRESS Polymer Letters, 6 (2012) 237-248.

[23] M. Othman, S. Hasan, S. Khamis, M. Ibrahim, S. Amin, Optimisation of Injection Moulding Parameter towards Shrinkage and Warpage for Polypropylene-Nanoclay-Gigantochloa Scortechinii Nanocomposites, in Advances in Material & Processing Technologies Conference. (2017) ScienceDirect.

[24] S. Khamis, M. Othman, S. Hasan, N. Main, S. Masrol, M. Shaari, S. Ibrahim, S. Salim, Multiple Responses Optimisation in Injection Moulding Parameter for Polypropylene-Nanoclay-Gigantochloa Scortechinii via Taguchi Method, in International Conference on Mechanical and Manufacturing Engineering. (2019), IOP.

[25] M. Othman, M. Rosli, S. Hasan, A. Amin, M. Hashim, O. Marwah, S. Amin, The Optimisation of Processing Condition for Injected Mould Polypropylene-Nanoclay-Gigantochloa Scortechinii based on Melt Flow Index. in IOP Conf. Series: Materials Science and Engineering. (2018) IOP.

[26] A. Shebani, W. Elhrari, A. Klash, A. Aswei, K. Omran, A. Rhab, Effects of Libyan Kaolin Clay on the Impact Strength Properties of High Density Polyethylene/clay nanocomposites, International Journal of Composites Materials, 6 (2016) 152-158.

[27] A. Shebani, W. Elhrari, A. Klash, A. Aswei, K. Omran, A. Rhab, High density polyethylene/Libyan Kaolin Clay Nanocomposites: Effect of Clay Particles Size on Rheological, Surface and Mechanical Peoperties. in First conference for engineering sciences and technology. (2018).

[28] A. Trish, W. Elhrari, H. Etmimi, A. Klash, Analysis of variance of injection moulding process parameters and clay particles size effects on impact strength, shrinkage and warpage of polyethylene/kaolin clay composites, Journal of Engineering and Applied Science, 69:112 (2022) 1-10.

Al-Mukhtar Journal of Engineering Research 07 (1): 12-19, 2023
Doi: https://doi.org/10.54172/jszswq55

Research Article

Open Access

A survivable Point-to-Point (PTP) Wireless Transmission Based On Adaptive Coding and Modulation (ACM) Technique

Ibrahim M M Mohamed*, Saif AL-Islam Ateeya AL-Salheen

***Corresponding author:** ibrahim.zalitny@omu.edu.ly
Electrical and Electronics Department, Faculty of engineering, Omar Al Mukhtar university, Libya

Second Author: ibrahim.zalitny@omu.edu.ly
Electrical and Electronics Department, Faculty of engineering, Omar Al Mukhtar university, Libya

Third Author: ibrahim.zalitny@omu.edu.ly,
Electrical and Electronics Department, Faculty of engineering, Omar Al Mukhtar university, Libya

Received:
25 May 2023

Accepted:
25 November 2023

Publish online:
31 December 2023

Abstract

Wireless transmission can be affected by severe weather conditions such as heavy rain. Such a temporary weather condition leads to decrease the received power and thus reduce the signal-to-noise ratio, which degrades the overall performance. In some cases in which a high bit rate is being transmitted where a specific amount of signal-to-noise ratio is required, the wireless transmission drops down completely. Adaptive Coding and Modulation technique could provide the feature of adaptation during transmission. In Adaptive Coding and Modulation, transmission parameters such as modulation scheme and/ or code rate can be altered based on signal-to-noise ratio measurements. In this paper, a survivable point-to-point wireless transmission was established using Adaptive Coding and Modulation technology. A concentration on the Adaptive Modulation was made in this work by using the AF-11FX equipment which is capable of modulate carriers using different modulation schemes (QPSK, 16QAM, 64QAM, 256QAM, and 1024QAM). In this context, the wireless point-to-point link was examined with and without the use of Adaptive Modulation. A survivable transmission was achieved in which an automatic switching mechanism is performed among the aforementioned modulation schemes based on signal-to-noise ratio measurements, which led to increase the average transmission rate.

Keywords: Wireless Transmission, Modulation Schemes, Coding Rate, Adaptive Coding, Adaptive Modulation

INTRODUCTION

The introduction should articulate the problem being addressed. It should provide sufficient background information on the subject allowing the reader to have more insight into what will be It has been known until a recent time that optical fibers are the most successful means of transmitting data at high rates due to their huge bandwidth. However, they will not remain the best in the near future due to the expected challenges in the next generations of communication networks [1]. One of the most important of these challenges is the large tendency of users to use smart phones along with the demand for broadband transmission. This challenge can be overcome if transmission and reception are activated wirelessly in the millimeter waves band. Another challenge arises here, which is the sensitivity of the millimeter waves band to severe weather conditions such as heavy rains. This might lead to cut-off transmissions when high data rates are sent where a certain amount of SNR is required. This problem can be settled if some type of adaptive transmission becomes available. In other words, transmission under severe

weather conditions can be maintained by automatically altering transmission parameters such as modulation and/ or code rate that require lower SNR value [2]. In this article a survivable wireless PTP transmission was realized over 11 km in a mountainous area. The implementation method was divided into two parts. The first part of the implementation method was based on simulation approach in which the web application tool was exploited to validate the feasibility of the 11 GHz band. Whereas the second part was based on experimental approach in which the technology of Adaptive Coding and Modulation (ACM) was involved. Followings are some related works found in the literature:

Satoshi et, al in [3] evaluated the performance of super high bit rate mobile communications using computer simulation at 11 GHz band 24×24 Multi-input, Multi-output MIMO outdoor propagation environment where an increase in the throughput exceeding 30 Gbps was achieved. The work in the above mentioned article also clarified the requirements for the average SNR, channel conditions, and accuracy of channel state information (CSI) for achieving 30 Gbps throughput over a real 11 GHz band 24×24 MIMO channel. However, an experimental solution have not been conducted due to hardware limitations. Kentaro et, al in [4] discussed the characteristics of 11 GHz band MIMO channel in a street micro-cell environment. The results showed that the scattered signal component was weak compared with measurement results of indoor environments. In addition, a further utilization for the MIMO channel modeling in the higher frequency band was expected. Y. Oda et, al in [5] presented outdoor wideband 8×8 MIMO channel measurements using dual-polarized antennas at 11 GHz. The measurements were conducted in the urban and residential areas of Ishigaki City, Okinawa, Japan. The effect of different polarizations on MIMO capacity and efficiency were estimated with respect to the dependency on local propagation environments. The results showed that there is a proportional increase in the capacity as the number of the antenna increases in non-line-of-sight environment.

Fresnel Zones Concept and Analysis

In wireless channels, a transmitted signal might take several paths before it reaches the receiver even in a line-of-sight environment. The parts of the signal that take paths other than the line-of-sight path, might subject to reflection before reaching their destination [6]. This would lead to destructive interference between the part of the signal that passes through the direct path and the other part that passes through the reflected path if the phase difference between the two parts is half an odd integer multiple of the period. The n-th Fresnel zone can be represented as a group of reflecting points that are located on three dimensional space such that a two segments path from the transmitter to the receiver that reflected off at any arbitrary point on that surface will be between n-1 and n half-wavelengths out of phase with the straight-line path. The shape of these zones are elliptical with foci at the transmitter and receiver. Fresnel zone analysis can help in designing a clear path between the transmitter and receiver. Obstructions within the first Fresnel zone can cause significant destructive interference and thus leads to weaken the received signal, even if those obstructions are not blocking the apparent line-of-sight path. Thus, it is required to determine the size of the 1st Fresnel zone to decide whether or not a noticeable signal weakness will take place. To realize an ideal 1st Fresnel zone, 80% of clearance is required. However, practically, not less than 60% of clearance is considered adequate [7] [8]. Consider an arbitrary point P at distances d_1 and d_2 with respect to each of the two antennas as shown in Figure 1.

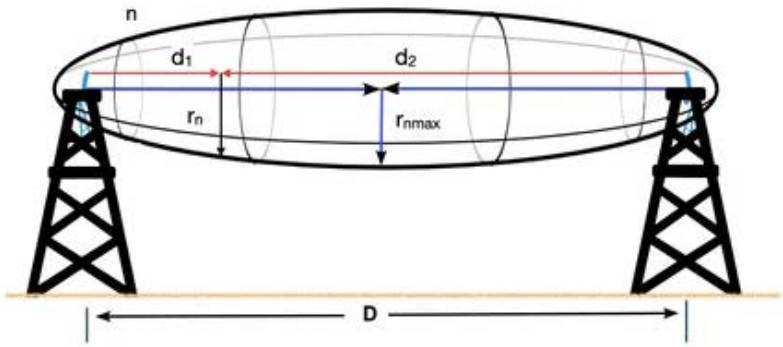

Fig.1 Schematic Representation of nth Fresnel Zone

To obtain the radius r_n of zone n, note that the volume of the zone is delimited by all points for which the difference in distances, between the direct wave ($D = d_1 + d_2$) and the reflected wave ($\overline{AP} + \overline{PB}$) is the constant n times half of the wavelength $\frac{\lambda}{2}$.

This can be represented mathematically as:

$$\overline{AP} + \overline{PB} - D = n\frac{\lambda}{2} \quad (1)$$

Re-writing (1) with the coordinates of point P and the distance between antennas gives:

$$\sqrt{d_1^2 + r_n^2} + \sqrt{d_2^2 + r_n^2} - (d_1 + d_2) = n\frac{\lambda}{2} \quad (2)$$

Doing more simplification in (2) gives

$$d_1\left[\sqrt{1 + \frac{r_n^2}{d_1^2}} - 1\right] + d_2\left[\sqrt{1 + \frac{r_n^2}{d_2^2}} - 1\right] = n\frac{\lambda}{2} \quad (3)$$

Assuming the distances between the antennas and the point P are much larger than the radius and applying the binomial approximation $(1+x)^{\alpha} \approx 1 + \alpha x$ for $x \ll 1$.

Doing the binomial approximation for the square root would simplify the expression to:

$$\frac{r_n^2}{2}\left[\frac{1}{d_1} + \frac{1}{d_2}\right] \approx n\frac{\lambda}{2} \quad (4)$$

solving (4) for r_n gives

$$r_n \approx \sqrt{n\frac{d_1 d_2}{D}\lambda}$$, where $d_1, d_2 \gg n\lambda$ (5)

Adaptive Coding and Modulation (ACM)

Rely on worst case scenario in designing any communication systems leads to inadequate utilization of available resources, whereas tolerance in the design would reduce the reliability [9]. For example, it is often intended to increase the capacity of wireless transmission while maintaining it available all the time, which is a very challenging issue. To solve this dilemma, ACM was introduced as a compromise which makes wireless transmission even more attractive. ACM technology seeks to realize adaptations during transmission by automatically altering some transmission parameters, such as modulation, code rate, or power based on feedback CSI [10]. More specifically, ACM refers to the automatic adjustment that a wireless system can make to resist weather-caused impairments that leads to fading and thus enhance the average rate of transmission. The idea is simply to make a frequent CSI at the receiver side and feed it back to the transmitter. As the transmitter receives the CSI, it alters its transmission parameters accordingly. In ACM-based transmission, the receiver sends back CSI to the transmitter via a feedback channel. The transmitter then adjusts its transmission parameters based on that CSI to maintain a survivable transmission. This scheme has the capability to significantly increase the spectral efficiency of wireless transmission. Figure 2 shows a basic ACM-based

wireless communication system.

Work Implementation

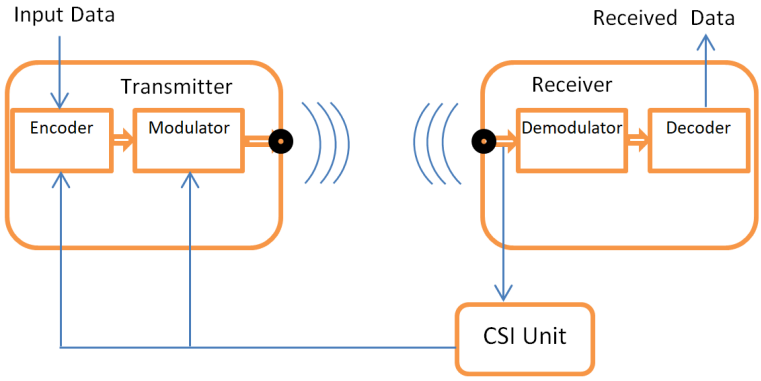

Fig. 2 A basic ACM-based wireless communication system

This section is divided into three parts. In the first part, an almost free of obstacles point-to-point link is established based on Fresnel Zone concept. In the second part, the channel capacity is estimated in case of using different types of modulation techniques. In the third part, the ACM is incorporated in the transmission process. As a part of preparing a clear Fresnel Zone, we entered the coordinates and height of the transmitter and receiver antennas using the web application. In this context, the positions of the transmitter and receiver antennas were 32.763989, 21.761985 and 32.806079, 21.870386, respectively, whereas, the height of the transmitter and receiver antennas were 42 m and 36 m, respectively. The antennas heights were entered with regardless of sea level altitude because it is included in the web application. The separation distance was calculated automatically by the web application which was 11.17 Km. The web application also suggested the use of 5 GHz band for transmission. Figure 3 shows the Fresnel Zone based on the recommended band. It is obvious from Figure 3 that the point-to-point link is not 100% clear. Based on the Fresnel Zone analysis, a reduction in radius can be achieved by increasing the frequency. Thus, we choose to increase the frequency to 11GHz and observe the situation via the web application.

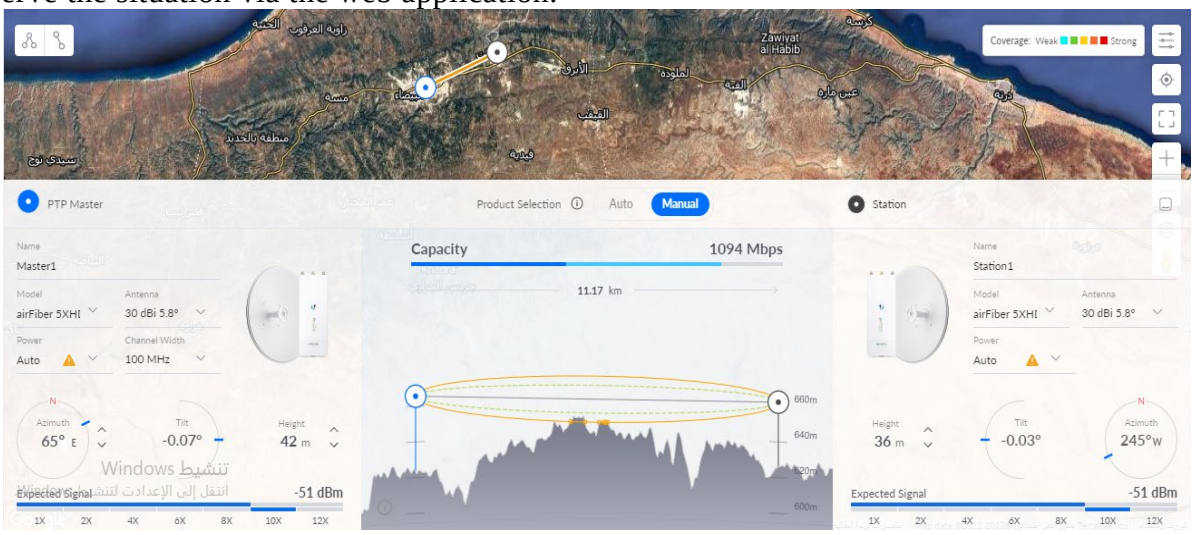

Fig.3 Fresnel Zone based on the 5 GHz recommended band by the web application

Figure 4 shows the Fresnel Zone when 11GHz is used where an almost free obstructions point-to-point link was achieved. The 11GHz band was chosen for the following reasons: (a) It is a part of the microwave bands that is devoted to the education sector, (b) It leads to a higher

channel capacity, (c) Moving to 11GHz band helps to avoid interfering with the license free and commonly used 5GHz band. The equipment (AF-11FX) has been installed on both sides of the point-to-point link to work as transceivers. This equipment has the capability to modulate carriers using QPSK, 16QAM, 64QAM, 256QAM, and 1024QAM.

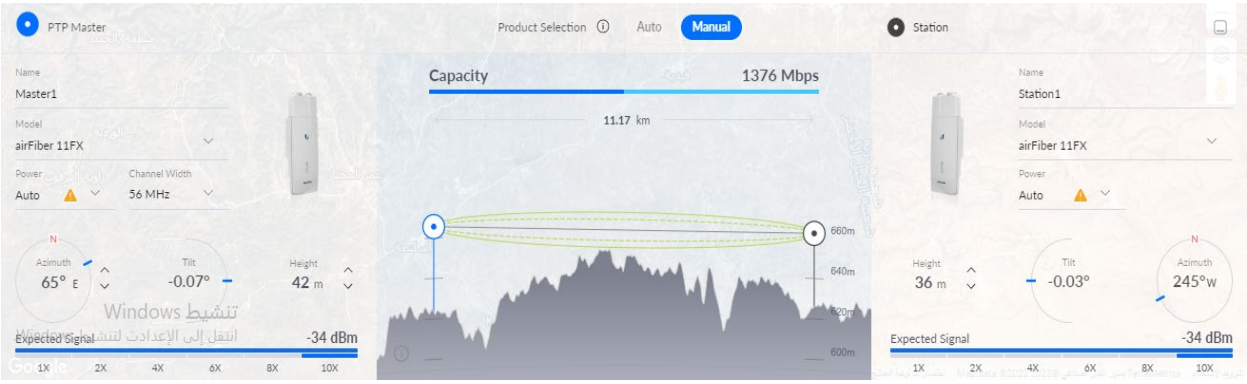

Fig.4 An almost free obstructions Fresnel Zone using 11 GHz

In addition, it is featured with ACM technology. To estimate the maximum channel capacity using the aforementioned modulation techniques, transmission was set using the following parameters:

- Tx frequency: 11060 MHz
- Rx frequency: 11550 MHz
- Channel Width: Max 56 MHz
- Modulation: QPSK, 16QAM, 64QAM, 256QAM, and 1024QAM
- Mode: MIMO
- Tx Power: 20 dBm
- Tx Antenna Gain: 35 dBi

The obtained measurements were listed in Table 1.

Table 1: Maximum channel capacity obtained using AF-11FX Equipment

Channel Bandwidth	Mode	Modulation Scheme	Capacity (Mbps)
56 MHz	MIMO	QPSK	137.6
		16 QAM	275.2
		64 QAM	412.8
		256 QAM	550.4
		1024 QAM	687.9

Based on the capacity measurements, one can choose to establish the link using the lowest capacity all the time to ensure high reliable transmission, however, this will come at the cost of the spectrum efficiency. On the other hand, if the link is establish using the highest capacity, it might be dropped down due to un expected weather conditions, such as rain, snow, or even fog. Here, the role of incorporating the ACM comes clearly. To do so, transmission was made while altering the modulation to the automatic rate adaptation mode. The power and gain values are altered several times to monitor the automatic adaptation of modulation rate. The flowchart in Figure 5 describes the ACM mechanism performed by the AF-11FX equipment.

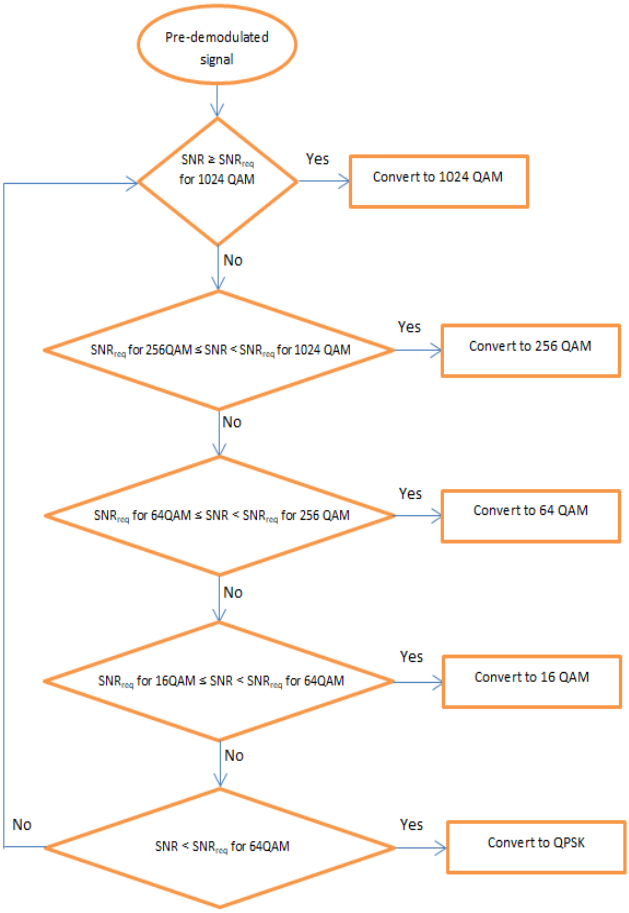

Fig.5 ACM mechanism using AF-11FX equipment

By observing Figures 6 and 7, one can easily extract the difference between the ACM-Free and ACM-Based transmissions. In the case of ACM-Free transmission, the link is going down if SNR lower than the required SNR is measured. ACM-Based transmission survive the link. In other word, the rate of modulation will be automatically changed depending on the link status, which led to increase the average capacity of the link.

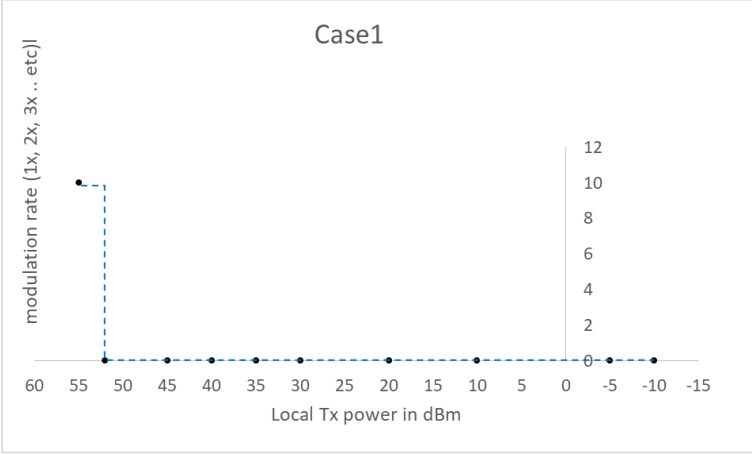

Fig.6 ACM-Free transmission

CONCLUSIONS

In this article a survivable wireless PTP transmission was implemented. The implemen-

tation was divided into two parts. In the first part, the web application simulation tool was exploited to validate the feasibility of the suggested 11 GHz band, whereas in the second part, the technology of ACM was experimentally involved. An improvement in the average capacity was achieved due the automatic switch among the employed modulation schemes rather than dropping the link down and getting zero capacity at severe weather conditions.

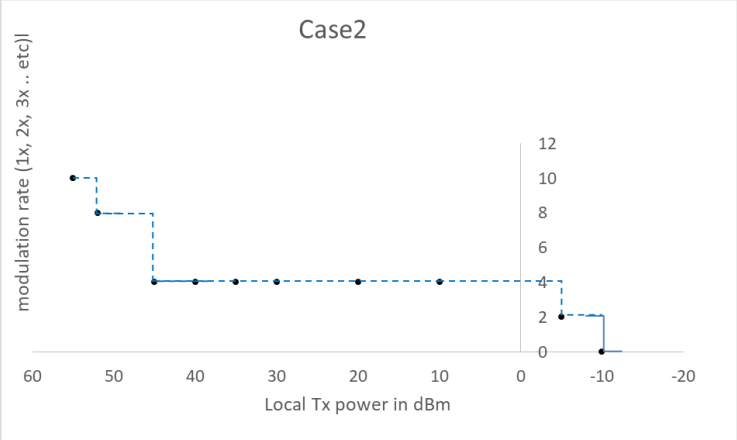

Fig.7 ACM-Based transmission

REFERENCES

[1] François Magne, Antonio Ramirez, and Claudio Paoloni, " Millimeter Wave Point to Multipoint for Affordable High Capacity Backhaul of Dense Cell Networks", 2018 IEEE Wireless Communications and Networking Conference (WCNC): Special Session Workshops, 978-1-5386-1734-2/18/$31.00 ©2018 IEEE

[2] Stefano Chinnici, Enrico Carni, Marco Manfredi, Leonardo Tufaro, Guido Montorsi, Sergio Benedetto, and Christian Camarda, " Design and Implementation of an Adaptive Coding and Modulation system for Microwave Radio Transmission in Mobile Backhaul Networks", 2014 8th International Symposium on Turbo Codes and Iterative Information Processing (ISTC), 978-1-4799-5985-3/14/$31.00 ©2014 IEEE

[3] S. Suyama, J. Shen, H. Suzuki, K. Fukawa and Y. Okumura, "Evaluation of 30 Gbps super high bit rate mobile communications using channel data in 11 GHz band 24×24 MIMO experiment," 2014 IEEE International Conference on Communications (ICC), Sydney, NSW, Australia, pp. 5203-5208, 2014, doi: 10.1109/ICC.2014.6884147.

[4] K. Saito, J. -i. Takada and M. Kim, "11 GHz band MIMO channel characteristics in a street micro-cell environment," 2017 11th European Conference on Antennas and Propagation (EUCAP), Paris, France, pp. 703-706, 2017, doi: 10.23919/EuCAP.2017.7928473.

[5] Y. Oda, J. Shen, N. Tran and T. Maruyama, "11 GHz dual-polarization MIMO channel measurements and capacity evaluation for mobile communications," 2013 IEEE-APS Topical Conference on Antennas and Propagation in Wireless Communications (APWC), Turin, Italy, pp. 295-298, 2013, doi: 10.1109/APWC.2013.6624883.

[6] Braasch, Michael S. "Multipath". Springer Handbook of Global Navigation Satellite Systems. Cham: Springer International Publishing. pp. 443–468, 2017.

[7] Coleman, Westcott, David, David, "Certified Wireless Network Administrator Official Study Guide", 111 River St. Hoboken, NJ 07030: John Wiley & Sons, Inc. p. 126. ISBN 978-1-118-26295-5, 2012.

[8] Fresnel Zone Clearance, https://www.softwright.com/faq/engineering/Fresnel%20Zone%20Clearance.html

[9] K. Fatima, S. Sheikh Muhammad, and Erich Leitgeb, " Adaptive Coded Modulation for FSO Links", 8th IEEE, IET International Symposium on Communication Systems, Networks and Digital Signal Processing, 978-1-4577-1473-3/12/$26.00 ©2012 IEEE

[10] Anshul Jaiswal, V. K. Jain, and Subrat Kar, " Adaptive Coding and Modulation (ACM) Technique for Performance Enhancement of FSO Link", 2016 IEEE First International Conference on Control, Measurement and Instrumentation (CMI), 978-1-4799-1769-3/16/$31.00 ©2016 IEEE

Al-Mukhtar Journal of Engineering Research 07 (1): 20-28, 2023
Doi: https://doi.org/10.54172/wadd2q70

Research Article **Open Access**

Development of Drag Coefficient Correlations for Circular Cylinder Using Turingbot Symbolic Regression Software

Husam A. Elghannay[(1)], and Yousef M. F. El Hasadi[(2)]

***Corresponding author:** E-mail addresses: example@example.com Department of Mechanical Engineering, University of Benghazi, Benghazi, Libya.

Second Author: E-mail addresses: example@example.com Frederik Hendrikstraat 2628 SX, Delft, the Netherlands

Received:
12 July 2023

Accepted:
26 November 2023

Publish online:
31 December 2023

Abstract

The current paper provides a symbolic regression-based correlation for the drag coefficient for circular cylinder. The correlation is intended to be applicable over a wide range of flow regimes namely that range from the creeping flow regime up to the turbulent flow regime. Demo version of TuringBot symbolic regression software was used to develop different correlations using different sets of data. Experimental set of data was used in one run whereas steady numerical results for Reynolds number up to ~ 25 were used in generating a second set of formulas. In a different run data generated using Sucker and Brauwer (Wärme-und Stoffübertragung, 1975. 8: p. 149-158) correlation with uniform distribution in each order of magnitude was used to obtain a different set of correlations. The data was generated across five orders of magnitude of change of Re. Among all suggested formulas in the three cases, four correlations are considered for their simplicity and accuracy. The predictions of the correlations ranged from reasonably good to very good as compared to existing data and correlations. The relative error of the four developed correlations ranged between 9% and 16% when compared to experimental data for Reynolds numbers ranging from 1-10^5. In particular, one correlation was able to capture all the qualitative and quantitative changes in the drag coefficient over the different flow regimes for $0.15 < Re < 10^5$. The relative error of this correlation was comparable to Sucker and Brauwer correlation.

Keywords: Drag Coefficient; Circular Cylinder; Correlation; Machine Learning; Symbolic Regression

INTRODUCTION

The flow over fully or partially submerged bluff bodies in a fluid flow has been of interest to a vast number of researchers for several decades ago. Early documented interests of the subject may date back to da Vinci (1513) whom sketched the flow patterns around a partially submerged columns [1]. First photographs of alternating vortices past a cylinder are those reported by Henri Bénard [2], a phenomenon that is known later by Kármán-Bénard Vortex Street. Besides investigating the flow patterns around submerged bodies, the resistance force (or drag force) felt by the objects as they move through the fluid is in the core of interests of researchers. The drag force and its behavior is crucial in the design of aerofoils, automobile bodies, buildings, and airspace shuttles. To allow for a comparison of different bodies at the same flow conditions, the drag force is typically non-

dimensionaized with respect to the kinetic energy of the incoming fluid resulting in the drag coefficient (C_D).

A fundamental case of interest is the case of a circular cylinder perpendicular to a steady stream. The flow pattern generated by the flow over the cylinder exhibits a rich mosaic of flow morphologies. The drag coefficient depends on how well the air flow around the object and leaves it. Streamlined shapes and small area shapes in the flow direction generally give lower values of the drag coefficient [3]. The flow disturbance caused by the cylinder is restricted to trailing wake downstream and significantly affects the drag force. The presence of alternating shedding from the cylinder produces an oscillatory lift force on the cylinder perpendicular to the stream motion[4]. The behavior of the flow around the cylinder changes dramatically with the change of Reynolds number (Re) and so does the drag force. Two different mechanisms contribute to the drag force, the skin friction and the form drag (or pressure drag). While the first (skin friction) is directly related to shear stresses on the surface of the surface, the second is a result of the pressure difference in the direction of the drag force [3, 5].

The variation of C_D with Reynolds number is shown in Figure 1 for circular cylinder across a range of Re from 10^{-1} to 10^7. The quantitative changes of the drag coefficients over this wide range of Reynolds number are associated with tremendous variations in the qualitative flow field aspects [5]. A thorough discussion of the different flow regimes can be found in [3, 6-8]. A brief review of the different regimes is provided here for reference with Figure (1) to facilitate associating the qualitative changes in C_D with physics of the problem. For very low values of Re, say, $Re < 4$, the flow is attached to the cylinder and the streamlines are almost symmetrical and come together as they pass over the cylinder. This is a direct result of high viscosity which dominates fluid inertia effects. This viscous flow regime is called Stokes flow. As Re is increased for up to 40, separation occurs on the aft of the cylinder forming two stable distinct vortices which are stationary in their place. The vortices become unstable beyond this limit and start alternate regular shedding at the wake region (called Karaman vortex street). Further increase in Re causes the Karman vortex street to turn into turbulent and later changes into a distinct wake ($150 < Re < 300$). The separation point of the boundary layer shifts towards the back of the cylinder along the surface with the transition to fully turbulent flow.

The drag coefficient remains at an almost constant value of about one at the range of $10^3 < Re < 3\times10^5$. Further increase in Re ($3\times10^5 < Re < 3\times10^6$) makes the flow in the outer region of the boundary layer to changes to turbulent flow causing reattachment followed by another separation of the boundary layer at the back face of the cylinder. As the flow changes to turbulent the wake thickness shrinks resulting in a reduction in the pressure drag on the cylinder to undergo a dramatic drop around $Re = 3\times10^5$ (also known as the drag crises). Beyond $Re > 3\times10^6$, a direct transition of the boundary layer to turbulent flow takes place at some point on the forward face. The separation of boundary layer at this case is estimated at an angular location slightly less than 120^o on the back surface. The separation points on the back surface shifts closer to the top and bottom of the cylinder, producing a thicker wake, thus larger pressure drag.

Three distinct flow regimes can be used to characterize the variations of the drag coefficient of the cylinder known as subcritical, supercritical and transcritical based on their location from the critical Re at which the drag crisis takes place. The roughness of the cylinder surface affects both the value of Re at which the drag crisis takes place and the value of the drag coefficient after the drag crisis. More details and investigations about the drag crisis can be found in [6, 10].

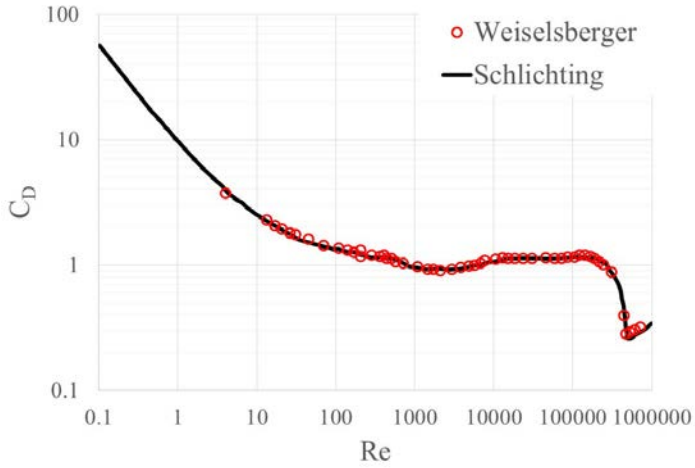

Fig. 1: Drag vs. Reynolds number for infinitely long circular cylinder (reproduced from [9]). Void circles are experiments made by Wieselsberger, the solid line is advised by Schlichting.

Qualitatively speaking the regimes and general shape of the C_D vs Re plot of flow over circular cylinder is similar to that of flow over a sphere. However, much more research is dedicated towards formulating a drag correlations for spherical particles compared to those for cylinders. Particles, bubbles, and droplets which are found in vast industrial and environmental systems can be reasonably approximated as spherical particles and hence come the significance of investigating spheres over cylinders. As a result the literature is saturated of correlations for drag over spheres which is yet worth further investigation. Symbolic regression was used to develop correlations of the drag over sphere by Baratti et al. [11] and El-Hasadi & Padding [12] using large volume of experimental data. Development of drag formula for spheroids and spherocylinder particles using limited size of high fidelity data using symbolic regression was also performed by El-Hasadi & Padding [13]. To the best of the authors' knowledge, no such use is reported to develop a correlation pertaining the drag over cylinder. The size of data used in the current work is not sizeable, but with no much notable variability.

A thorough review of all the existing correlations and experimental data is beyond the scope of this work and can be found in [9, 14, 15]. Selected correlations which includes the most commonly used in relevant literature are first outlined in the next section and their agreement with most common experimental data is reviewed. The software used in the current work is presented in section and selected correlations obtained by the software are presented in section 3. A discussion of the performance and limitations of the found formulas is provided in section 3 as well.

1. METHODOLOGY

1.1 Review of existing data and correlations

Stokes pioneered investigating the flow over spheres and cylinder at very low Re (also called creeping flow regime Re <<1). Stokes analytically solved the steady drag over a sphere in infinite medium but stated that no solution exists in flow over cylinders [16]. His postulate triggered a researchers to perform theoretical and experimental studies with varying qualitative and quantitative agreement [17]. The unclearness of the data is not well defined in many cases leading to conflicting sets of data that requires careful reevaluation and attempts to correct [18].

One of the most commonly used correlations is that of Kaplun [19] whom used matched asymptotic expansion to improve the approximate solution provided by lamb [20] to Stokes paradox

$$C_D = \frac{8\pi}{Re}\left[\left(ln\left(\frac{7.406}{Re}\right)\right)^{-1} - 0.87\left(ln\left(\frac{7.406}{Re}\right)\right)^{2}\right] \quad (1)$$

Reynolds number herein is based on the diameter of the cylinder. The formula diverges for Re values >1. White [14] offered a simple curve-fit formula which is reasonable agreement up to the drag crisis (Re < 250000). The data used in generating the correlation are from Tritton [21] and Wieselesberger [22]

$$C_D = 1 + \frac{10}{Re^{2/3}} \quad (2)$$

A roughly derived formula is suggested by Munson et al. [3] in which separation of the boundary layer is assumed to take place at 109° (measured from stagnation point).

$$C_D = 1.17 + \frac{5.93}{\sqrt{Re}} \quad (3)$$

The first term on the RHS comes from form drag while the second represents skin friction. The skin friction term was assumed to have similar dependencies between C_D and Re as that of a flat plate.

An accurate curve-fit formula [14] was proposed by Sucker & Brauwer [23]

$$C_D = 1.18 + \frac{6.8}{Re^{0.89}} + \frac{1.96}{\sqrt{Re}} - \frac{0.0004Re}{1 + 3.63 \times 10^{-7}Re^2} \quad (4)$$

Mapping of the above correlations on C_D vs. Re diagram that contains a compilation of existing data as made by Panton [7] is provided in Figure (2). The steady numerical (blue dashed line) results line is for steady numerical results by Hamielec and Raal (1969) [24] and Fornberg [25] assuming steady flow. Kaplun correlation (Eq. (1)) diverges for Re >1 while Munson's correlation (Eq. (2)) may be applied to up to Re ~ 3×10^5. Munson's formula shows reasonable agreement for $2 > Re > 10^4$ but shows a different "slope" when plotted on a log-log scale of the C_D vs. Re plot. Although predictions of White's formula (Eq. (2)) is superior to that of Munson's, it fails to capture the minimum C_D value at $10^3 < Re < 10^4$. Sucker and Brauwer's formula (Eq. (4)) outperforms all the presented correlations and captures almost all qualitative behaviors before the drag crisis.

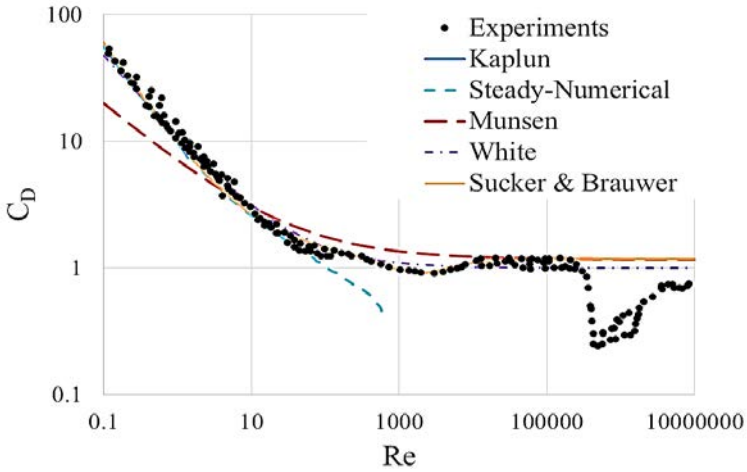

Fig. 2: Comparison of different correlations with experimental data for drag over circular cylinder. Experimental data compiled by Panton [7]**.**

1.2 Analysis Software

TuringBot symbolic regression software is chosen to perform the regression task. The free Demo version, however, has a limitation on both the number of data points and the number of inde-

pendent variables. The maximum number of data points is 50 whereas a variable can only be a function of other two parameters. Once the data is loaded, the target parameter along with the ratio of test/train sets is selected before running the job. It is optional to shuffle the data before running the job. Although the software defaults the parameter used to evaluate the accuracy to the root mean square (*rms*) value of the target variable, it is possible to select different criterion from a dropdown list. Once the task is executed, the software suggests a list of possible fitting functions (starting from a bare average). The software keeps refining (or replacing) the proposed formulas producing more accurate fits until the user decides to halt it. TuringBot interface allows for visualization of the different suggested solutions and how they fit the original data. Since the current work assumes $C_D=f(Re)$, the Demo version is appropriate given that the used data does not include much uncertainty.

2. RESULTS AND DISCUSSIONS

Selected sets of data were used to generate a drag formula and led to the following formulas:

$$C_D = \left(9.29 - shin^{-1}(3.19 - 0.000545Re)\right)/shin^{-1}(Re) \quad (5)$$

$$C_D = 1.268 + \frac{8.39}{Re^{0.82}} \quad (6)$$

$$C_D = 1.074 + \frac{8.76}{Re^{0.743}} \quad (7)$$

$$C_D = 1.154 + \frac{8.02 - 4.657 \times 10^{-5} Re^2}{(Re - 0.119)^{0.7229} + 6.601 \times 10^{-5} Re} \quad (8)$$

Data from Wieselsberger [22] at Re ranges from ~ 4 -105000 was used to generate Eq. (5) thus excluding the drag crisis experimental data. The data is a subset of the data in Figure 2 and is displayed in Figure 1. Although hyperbolic functions are not commonly used in drag formulas, Barati's correlation [11] for drag over sphere is rich of trigonometric and hyperbolic functions. It is not clear to us at the time being if these functions can actually be linked to the physics of the problem or they exist because of their ability to fit complicated behavior. The steady numerical results of Hamieleec & Raal [24] and Fornberg [25] are found to be in very good agreement with the average experimental data trend line advised by Schlichting (see Figure (1)) until Re ~25 [9]. Beyond Re ~25 deviations between the steady simulations and the experiment take place possibly because unsteadiness is initiated in the form of vortex shedding. The line at which the steady results almost match the experimental results was digitized to ~ 50 data points ($0.24 < Re < 24$) which were fed to TuringBot to generate Eq. (6). The third data set was generated using Sucker and Brauwer's correlation (Eq. (4)) for ($0.1 < Re < 10^5$) with equal number of data points in each order of magnitude. In the first two runs 75/25 test/train ratio was selected, however, all the data was used in the training (no testing) when Eqs. (7 & 8) were obtained. The former strategy of not spending part of the data in testing the trained model was adapted to ensure having equal weights for the different regimes in generating the correlation.

Comparison of Eqs. (5 - 8) is shown in the Figure (3). Eq. (5) shows some deviation at very low Reynolds number most likely because of the uncertainty in the data point used at Re~4 which affected the extrapolation process at lower Reynolds number values. On the other hand Eq. (6) shows quite good agreement for flow regimes before the drag crisis. Similar to the correlation by White (Eq. (2)), the physics embedded in the minimum Re at $10^3 < Re < 10^4$ are, however, not captured. Due to the relatively low number of data points at this region, it would be hard for the algorithm to capture the trend in this regime. Such drawback is avoided in the third set of data in which the data is generated in similar distribution at each "decade". Eq. (7) has similar structure to Eq. (6) which

comes from steady data but better agreement with experimental data at high Reynolds number. Both correlations converge to a constant value of C_D at high Re values ($Re > 10^3$). As can be seen from the equation itself, Eq. (7) converges to a value of 1.074 which is very close to the suggested value of one by White (Eq. 6). This Reynolds number-free term can be linked to the form drag as outlined by Munson et al. [3] and the value to which it converged could be linked to the separation angle of the boundary layer. The separation angle as a function of Re is a subject of interest to many researchers (e.g.[26, 27]).

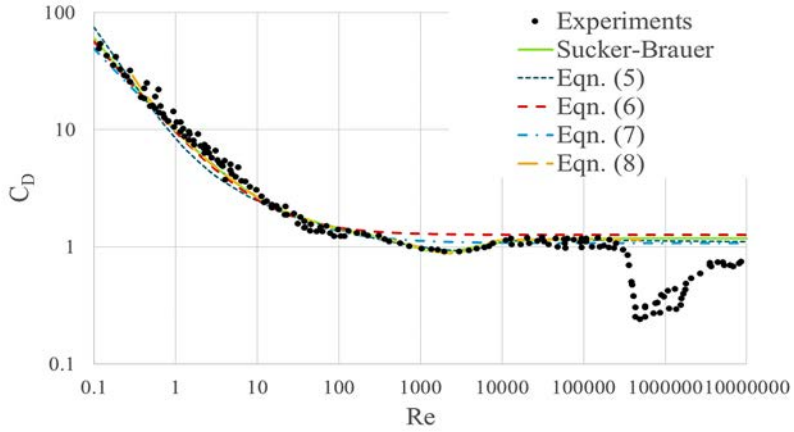

Figure 3. Comparison of the current results with available experimental data and empirical correlation of Sucker and Brauwer [23]

Table (1) lists the *rms* error for the proposed equations against the data used in testing, and the average relative error from the data of Wieslesbrger and finally against the available experimental data at Re ranges from ~1-10^5. All suggested correlations have low average rms error in their training data. When compared to Wielesberger experimental data which is used to generate Eq. (5) the relative error was the least for Eq. (5), however, Eq. (8) show comparable performance. Although Eq. (6) shows the highest deviations of ~16%, its deviation is not bad provided that it was generated using steady results for up to Re ~24. When the experimental data over a wide range is considered, Eq. (7) become comparable to both Eqs. (8) and Sucker and Brauwer (Eq. (4)). The relatively large error is mainly because of the variations of the results of the experimental data itself. The inability of Eq. (7) to capture the behavior at $10^3 < Re < 10^4$ is alleviated as a consequence of the limited number of data at that regime as compared to the total number of data points used. The performance of Eq. (5) now deteriorated as it diverges outside its training data regime. Indeed Eq. (8) has the best agreement among all obtained correlation over the wide range of Re. The local minimum is captured and the agreement with Sucker-Bauwer's correlation is obvious. Interestingly the correlation has consistently shown somewhat lower relative error when compared to the experimental data. The correlation, however, diverges beyond Re values lower than ~0.12 possibly because of the existence of negative number (at the denominator) raised to a negative number.

Table (1). Comparison of relative average error of proposed correlations with experimental data

Formula	Average rms error in training data	Average relative error %	
		Wieselsbrger	All Available
Eq. (5)	0.0477752	2.37	13.26
Eq. (6)	0.0728236	15.9	16.07
Eq. (7)	0.088027	6.3	9.83
Eq. (8)	0.0237282	2.89	9.15
S&B	NA	3.14	9.51

A close view of the performance of different correlations at low Re values is provided in Figure (4) for 0.1< Re < 10. It can be seen that White's correlation has the best agreement with experimental data at for 1 < Re <10. The correlation however underpredicts the experiments at lower values of Re and may depart at further low values. Equation (8) is in very good agreement with Sucker and Brauwer's formula and the steady numerical results.

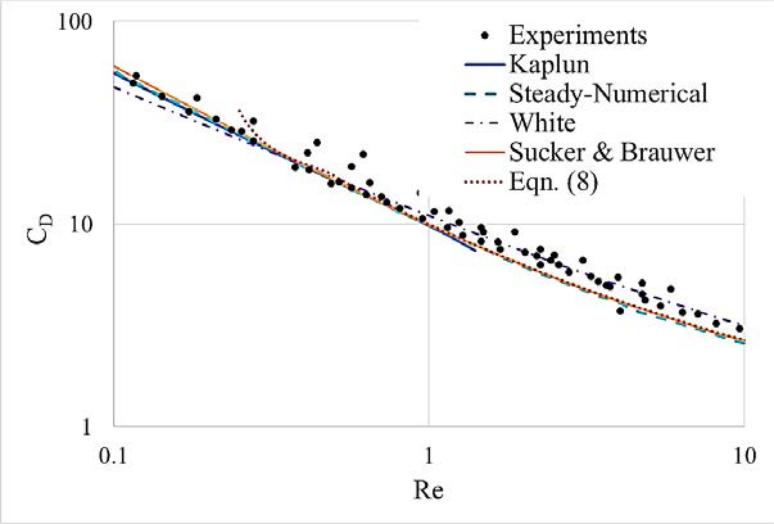

Fig. 4: Comparison of best correlations with experimental data at low Re values

3. Conclusions and Recommendations for Further Work

Symbolic regression was successfully used to generate a correlation that predict the drag coefficient for a wide range of Reynolds number. Although the developed correlation captured all the qualitative changes in C_D in the different flow regimes it does not extrapolate beyond the training regime used. In fact none of the existing correlations as of yet was capable of predicting the behavior at the drag crisis. The obtained correlation was developed by generating a reasonably small set of data from reliable correlation. The former strategy was adapted by El-Hasadi and Padding [12] in investigating the existence of logarithmic terms in the drag over sphere and is the best recommended in the absence of highly accurate measurements that covers the whole regime. Further investigation is required in the creeping flow regime if Stokes paradox is to be tackled using symbolic regression. Investigation of the existence of logarithmic terms and whether it is possible to predict the drag crisis in a generic formula are other research extensions that would be carried out using symbolic regression. For the former purpose, larger volume of data may be required.

REFERENCES

[1] Forouzi Feshalami, B., S. He, F. Scarano, L. Gan, and C. Morton, A review of experiments on stationary bluff body wakes. Physics of Fluids, 2022. 34(1): p. 011301.

[2] Bénard, H., Formation des centres de giration à l'arrière d'un obstacle en mouvement. Compt. rend., 1908. 147: p. 839.

[3] Munson, B.R., D.F. Young, and T.H. Okiishi, Fundamentals of fluid mechanics. Oceanographic Literature Review, 1995. 10(42): p. 831.

[4] Pritchard, P.J. and J.W. Mitchell, Fox and McDonald's introduction to fluid mechanics. 2016: John Wiley & Sons.

[5] Thom, A., The boundary layer of the front portion of a cylinder. 1928, HM Stationery Office.

[6] Anderson, J., EBOOK: Fundamentals of Aerodynamics (SI units). 2011: McGraw hill.

[7] Panton, R.L., Incompressible flow. 2013: John Wiley & Sons.

[8] Markland, E., A first course in air flow. 1976: Tecquipment limited.

[9] Schlichting, H. and J. Kestin, Boundary layer theory. Vol. 121. 1961: Springer.

[10] Kreith, F., Fluid mechanics. 1999: CRC press.

[11] Barati, R., S.A.A.S. Neyshabouri, and G. Ahmadi, Development of empirical models with high accuracy for estimation of drag coefficient of flow around a smooth sphere: An evolutionary approach. Powder Technology, 2014. 257: p. 11-19.

[12] El Hasadi, Y.M. and J.T. Padding, Do logarithmic terms exist in the drag coefficient of a single sphere at high Reynolds numbers? Chemical Engineering Science, 2023. 265: p. 118195.

[13] El Hasadi, Y.M. and J.T. Padding, Solving fluid flow problems using semi-supervised symbolic regression on sparse data. AIP Advances, 2019. 9(11): p. 115218.

[14] White, F.M. and J. Majdalani, Viscous fluid flow. Vol. 3. 2006: McGraw-Hill New York.

[15] Niemann, H.-J. and N. Hölscher, A review of recent experiments on the flow past circular cylinders. Journal of Wind Engineering and Industrial Aerodynamics, 1990. 33(1-2): p. 197-209.

[16] Stokes, G.G., On the effect of the internal friction of fluids on the motion of pendulums. 1851.

[17] Khalili, A. and B. Liu, Stokes' paradox: creeping flow past a two-dimensional cylinder in an infinite domain. Journal of Fluid Mechanics, 2017. 817: p. 374-387.

[18] Lienhard, J.H., Synopsis of lift, drag, and vortex frequency data for rigid circular cylinders. Vol. 300. 1966: Technical Extension Service, Washington State University Pullman, WA.

[19] Kaplun, S., Low Reynolds number flow past a circular cylinder. Journal of Mathematics and Mechanics, 1957: p. 595-603.

[20] Lamb, H., Hydrodynamics. 1924: University Press.

[21] Tritton, D.J., Experiments on the flow past a circular cylinder at low Reynolds numbers. Journal of Fluid Mechanics, 1959. 6(4): p. 547-567.

[22] Wieselsberger, C., New data on the laws of fluid resistance. 1922.

[23] Sucker, D. and H. Brauer, Investigation of the flow around transverse cylinders. Wärme-und Stoffübertragung, 1975. 8: p. 149-158.

[24] Hamielec, A. and J. Raal, Numerical studies of viscous flow around circular cylinders. The physics of fluids, 1969. 12(1): p. 11-17.

[25] Fornberg, B., A numerical study of steady viscous flow past a circular cylinder. Journal of Fluid Mechanics, 1980. 98(4): p. 819-855.

[26] Wu, M.-H., C.-Y. Wen, R.-H. Yen, M.-C. Weng, and A.-B. Wang, Experimental and numerical study of the separation angle for flow around a circular cylinder at low Reynolds number. Journal of Fluid Mechanics, 2004. 515: p. 233-260.

[27] Islam, T., S.R. Hassan, and M. Ali, Flow separation phenomena for steady flow over a circular cylinder at low Reynolds number. International Journal of Automotive and Mechanical Engineering, 2013. 8: p. 1406.

Al-Mukhtar Journal of Engineering Research 07 (1): 29-42, 2023
Doi: https://doi.org/10.54172/xs0k3530

Research Article **Open Access**

Vibration damping using granular materials

Saleh S. H. Emtaubel [(1)], Galal Hamed Senussi [(2)], Jim A. Rongong [(3)]

***Corresponding author:** saleh.emtobel@omu.edu.ly
Faculty of Mechanical Engineering, Omar Al Mukhtar university, Libya.

Second Author: , jalal.senussi@omu.edu.ly
Faculty of Mechanical Engineering, Omar Al Mukhtar university, Libya

Third Author: j.a.rongong@sheffield.ac.uk, Faculty of Mechanical Engineering, University of Sheffield, UK

Received:
17 July 2023

Accepted:
30 November 2023

Publish online:
31 December 2023

Abstract

The aim of this paper is to study experimentally and numerically the effects of vibration amplitude and frequency on the performance of granular systems, with a view to optimizing their use in reducing vibrations typically experienced in machinery. Granular material systems are highly nonlinear systems and, as such, have multiple factors that will affect any experiment. This nature of granular material systems caused some discrepancies between experiment results and the simulations of mathematical models. However, the nonlinear aspect of particle damping restricted researching its theory, but the experiment research has largely surmounted that limitation. Experimental results suggested several damping theories. Accordingly, the ability to reduce vibrations of particle dampers depends on several external and internal factors. The two external factors are excitation amplitude and its frequency, whereas the internal factors are related to the properties of the particles and the size of the container. Other internal factors relate to the mass ratio of total particles to the primary structure and particle placement. The experimental work included developing a computational single degree of freedom (SDOF) model to provide better understanding of the effect of shock vibration and work with the future experimental work.

Keywords: Damper, Vibration, Excitation, Frequency, beam.

INTRODUCTION

Particle dampers are devices that control vibration levels in structures. They function by an impact and friction damping together. The primary structure's energy is transferred to the particles inside the damper's casing that is attached to the vibrating system where it dissipated by being absorbed by the action of the contacts between the particles. The principal processes engaged in energy dissipating are collisions, sliding friction and rolling friction with those processes taking place between the particles and with the particles and the damper casing's walls. This type of damping can be optimized by adjusting the acceleration of the particles within the container [1]. At lower frequencies, the damping mechanism requires that the particles and the casing wall to be out-of-phase with one another resulting in comparatively empty container. Particle impact dampers originated from impact dampers and they are more efficient in reducing vibrations than them [2]. Another key mechanism operating inside particle dampers is associated with the granular material's state of matter. For example, at high amplitude frequencies gas-like states occur whereas at lower frequencies solid and liquid-like states appear. In this damping mechanism, performance can be optimized by paying attention to the state of the particles in the container [3].

Particle dampers are used in several industries to limit vibrations and noises. The aerospace industry led the way in using them, however; other industries such as automotive, medical and energy soon followed [4]. There are many particle dampers' applications in strengthening buildings against earthquake and in automotive gears to suppress vibrations in the rotary shaft of gear transmission. There are other uses in helicopter and aircraft mechanisms in rotor blades and landing gears, and in machine tools. Noise resulting from machine actions can also be reduced by impact dampers [5], however; at times the actions of the impact dampers can increase it [2].

The use of granular materials to reduce resonant vibrations in machinery and structures is increasing. They are attractive because they combine several different energy dissipation mechanisms, making them more versatile than traditional damping materials. This study sets out to understand and model the effects of vibration amplitude and frequency on the performance of granular systems, with a view to explaining and optimizing their use in reducing vibrations typically experienced in machinery.

Numerical modelling will be used alongside laboratory experiments to investigate the effects on energy dissipation performance of features such as particle material, shape, and the geometry of a flexible–walled packet container. The experiments described in this study were devised to give some introductory understanding of single particle damping. They were also intended to identify key variables and to direct the design of future experiments. The experiment was to investigate the damping performance of a single particle (viscoelastic sphere) placed within a cavity attached to a vibrating beam. First, the resonance of the beam plus empty damper was considered and then the natural frequency and modal damping ratio for different amplitudes and damper gap settings are identified.

Finally, the SDOF mathematical model is used to write a MATLAB code for a simulation to estimates time domain response for a SDOF impact damper using measured parameters obtained and the numerical results are then compared with the single particle impact damper experimental results.

MATERIALS AND METHODS

This experiment Investigated the resonance of a beam with a single damper attached and identified the first natural frequency and modal damping ratio for different amplitudes. The experimental analysis is performed with the system shown in figure 1.

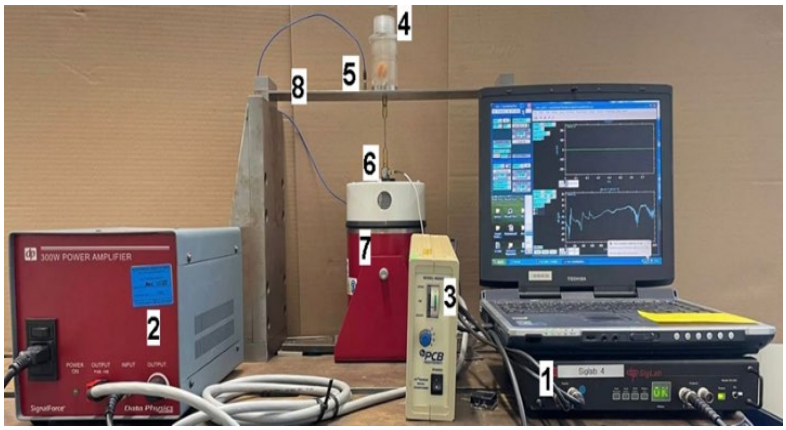

Fig. 1 Impact damper experiment setup

Table (1): Description of individual components

	SigLab 4 signal analyser
	300W power amplifier
	PCB model 482A22 charge amplifier
	Particle damping enclosure (empty)
	PCB 353B18 accelerometer (Sensitivity 981 m/s^2/V)
	PCB 208B01 force transducer (Sensitivity 8.99 N/V)
	Electromagnetic shaker (peak sine force capacity 100 N)
	Clamped steel beam 425L x 75W x 4D (mm)

The test structure is a steel beam that is clamped at either end. The beam has a cross-section that is approximately 75x4 mm and the free length between the clamps is approximately 425 mm. A casing of the damper (of mass 266.6 grams) is attached to the beam using a threaded connector.

The system is excited by an electrodynamic shaker via a stinger rod. The force applied by the exciter is measured with a force transducer and the beam vibration is measured with an accelerometer. Signals from these transducers are recorded on a data acquisition system (Table 1, Fig. 2). The test rig is adjusted such that the direction of shaking aligns with the direction of gravity. The vibration response is measured over a frequency range of around 10-1000 Hz using signals of varying magnitude and frequency content. The amplitude will be in the range 1 to 1000 m/s^2.

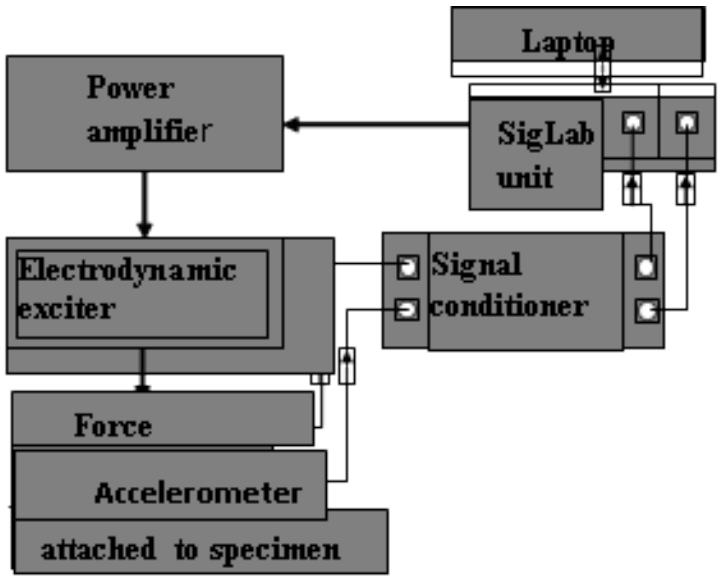

Fig. (2) Signal flow diagram

The impact damper's container as shown in Fig. 3 is similar to the damper used by Wong et al. [6]. It is constructed from a clear PMMA cylinder so the movement of the sphere can be noticed with a steel base. The container has a threaded top for gap size adjustment. A viscoelastic sphere(rubber) of mass 11.5 grams and diameter ≈ 25mm is placed in the container.

Natural frequency (ω_n) and damping ratio (ζ) measurements of the system were taken at gap sizes of 0 (lid firmly on top of sphere), 10, 15, 23 millimeters; and for random excitation 19 values of acceleration with an increment of 0.1g at accelerations of 0.07 to 1.7 g and for sin-ewave excitation 19 values of excitation acceleration with an increment of 0.1g from 0.05 to 5.0

g.

For random excitation, the SigLab virtual network analyzer (vna) was used which provides links to network-based analysis tools for measuring frequency response functions. Information was retrieved from (vna) data file, then the post process was done in the MATLAB setting using the SLm data structure using the MATLAB function frf_from_vna in

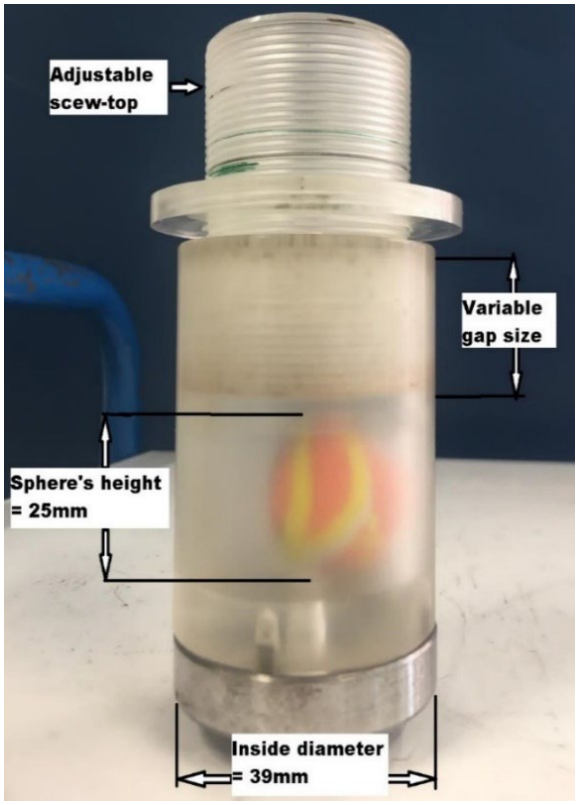

Fig (3). Damper container with adjustable gap

combination with the function from_frf to get the natural frequency and damping ratio from frf uses functions mobfit and mobfit_obj to curve fit. For sinewave excitation from the SigLab swept-sine analyzer (vss) was used for measuring the system's frequency response function. The data processing was done sing the MATLAB function frf_from_vss.

As for the repeatability and uncertainty in the results, there is a major problem connected with random excitation is that signals will always experience leakage. This leakage error will cause a serious reduction of the quality of the measured frequency response function (frf), with a sizable error resulting, mainly at the resonant peaks of the system **[7]**. Leakage is also an issue for sinewave excitation.

RESULTS AND DISCUSSION

Vibrating beam's natural frequency and modal damping ratio

First, the resonance of a vibrating beam is investigated and the natural frequency and modal damping ratio (ζ) for different amplitudes are identified. There is a difference in the damping ratio (ζ) trend between the different excitations as the damping ratio for random excitation is almost constant with the increasing amplitude whereas the damping ratio for sinewave excitation increases with the increasing amplitude (Fig. 4).

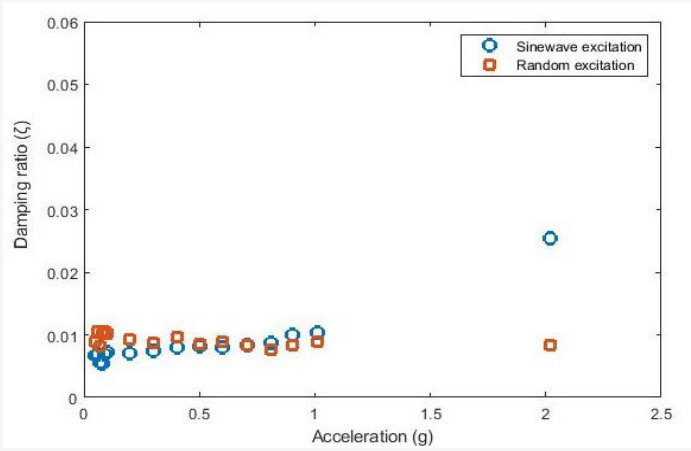

Fig. (4). The acceleration's (g) effect of on the damping ratio (ζ) for random and sinewave excitations

The results of the natural frequency (ω_n) for the different excitations are illustrated in fig. 5, where the beam response to random and sinewave excitation show the same trend.

If there is a resistance to the vibrations when the system is undamped then the system undergoes frictional or other type of loss of kinetic energy which is damped with time. The energy loss within the structure itself is called structural (hysteresis) damping where in solids some of the energy involved is the repetitive internal deformation and restoration to the original shape is dissipated in the form of random vibrations of an intramolecular nature. Most likely this is friction damping at the joints since metals have a loss factor of less than 0.001 and the PMMA damper does not significantly deform in the 10-100 Hz range.

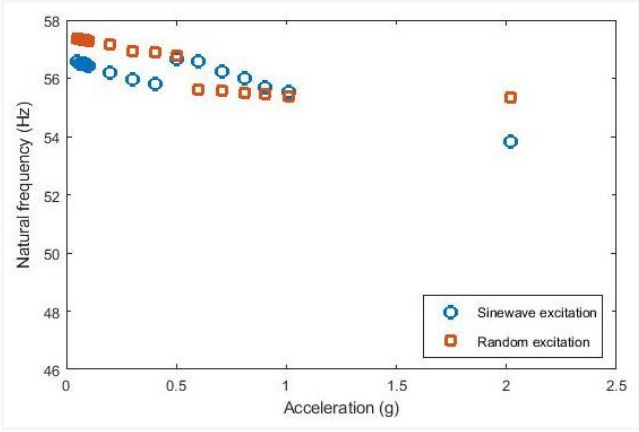

Fig. (5) Comparison of the acceleration's (g) effect of on natural frequency (ω_n) for random and sinewave excitations of a steel beam

The effects of gap size of an impact damper under random and sinewave excitation

When a continuous structure vibrates with a particular deflection shape, its motion can be represented by a SDOF system. The mass of this equivalent system is obtained using the equivalent kinetic energy. For slender uniform beams, the equations for normal vibration mode shapes are given in textbooks [8]. For these, they also show that for equal kinetic energy in both systems,

$$\frac{1}{2}\dot{y}_{SDOF}^2 m_{eq} = \frac{1}{2}\dot{q}^2 m \quad \Rightarrow \frac{1}{2}\dot{y}_{SDOF}^2 m_{eq} = \frac{1}{2}\left(\frac{y_{SDOF}}{\phi_i}\right)^2 m$$

where φ defines the shape of the deflection as a function of the distance along the beam and therefore,

$$m_{eq} = \frac{m}{\phi_i^2}$$

At the end of a cantilever the fundamental vibration mode shape gives $\varphi^2 = 4$, at the mid-point of a clamped-clamped beam $\varphi^2 = 2.52$ and at the mid-point for a pinned-pinned beam $\varphi^2 = 1$.

The beam has a cross-section that is approximately 75x4 mm and the free length between the clamps is approximately 425 mm.

The test structure is a steel beam that is clamped V= (L) (H) (W)

V = (0.425) (0.075) (0.004)

$= 1.275 \times 10^{-4}\ m^3$

ρ (For steel) = 7900 kg/m^3

The mass, m = (v) (ρ)

$= (1.275 \times 10^{-4}\ m^3)\ (7900\ kg/m^3)$

$= 1.00725$ kg

At the mid-point of a clamped-clamped beam $\varphi^2 = 2.52$

$$m_{eq} = \frac{m}{\phi_i^2}$$

$$= \frac{1.00725}{2.52}$$

$$= 399.7\ g$$

The mass of sphere = 11.5 g

The mass of empty container = 266.6 g

So, The Total mass is:

m_t =11.5 + 266.6 +399.7

= 677.8 g

First there is a discussion of random excitation results followed by the sinewave results. When the system is subjected to random excitation and for a gap size of 0 mm, even though the sphere does not have any space to move and this does not allow for significant interchange of momentum between the sphere and the container, the nature of random excitation high frequency causes the particle to have more movement. Therefore, it has dissipation of energy and the measured damping ratio is higher than 23 mm and 10 mm gaps (Fig. 6). As the gap size increases, the particles are given more room to move and the damping ratio (ζ) reaches 0.04104 at acceleration amplitude 1.7g which occurs at an optimum gap size of 15 mm. If the gap size is increased further there will be fewer impacts since the particle does not acquire enough velocity to travel from bottom of the container to the top, on the average twice per "cycle" of the response. Therefore, if the gap size is increased beyond the optimum, the damping decreases.

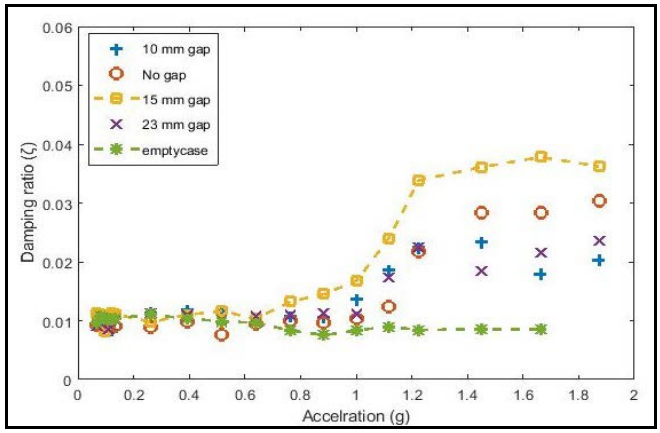

Fig. (6). The effect of acceleration g (rms) on the different gaps of an impact damper's damping ratio (ζ) under random wave excitation

The damping ratio at optimum gap size increases with increasing acceleration. Overall, the damping ratio of the beam was increased by over five times, demonstrating the effectiveness of the particle impact damper particularly at high amplitudes of excitation (Fig. 7). Experiments also revealed a shift in the resonance frequency of the system. This frequency shift is affected by both acceleration and gap size. Figure 8 shows that the resonance frequency decreases with increasing acceleration

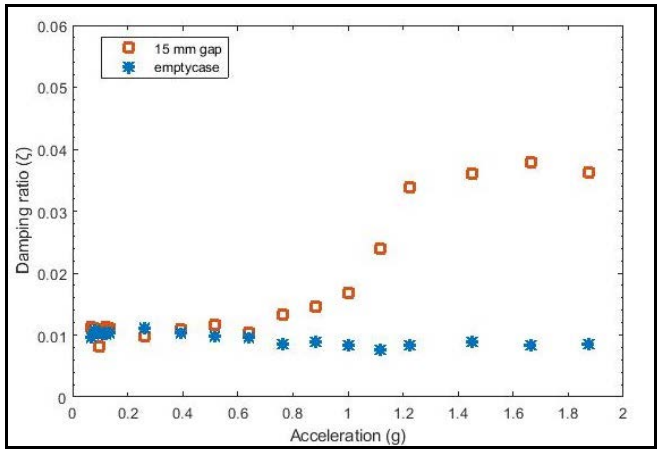

Fig. (7) Comparison of the acceleration g (rms) effect on the damping ratio (ζ) of an impact damper (with 15mm gap) to that of an empty-case under random wave excitation

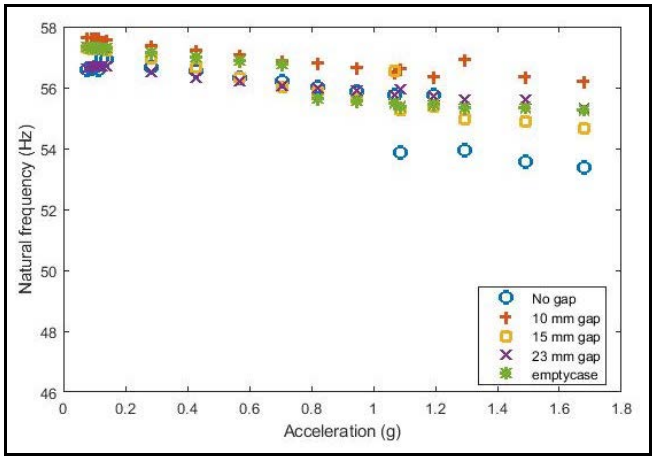

Fig. (8) The effect of acceleration g (rms) on the different gaps of an impact damper's natural frequency (ω_n) under random wave excitation

for all gap sizes at different rates. This confirms that as the sphere has more space to move, it contacts the container less resulting in a lower mass effect and higher resonance frequency. With the increase of acceleration, a higher mass effect is produced, which implies that the sphere has more contacts with the container. Overall, the natural frequency of 15 mm gap under random excitation is lower than that of the beam's natural frequency.

The damping ratio (ζ) values of the system under sinewave excitation exhibits show almost the same trend with the different gaps as the random excitation with the exception that the effective damper's gap is 10 mm which is smaller than that determined by random excitation (Fig. 9). The damping ratio of this gap is more than three times higher than that of the empty-case's damping (Fig. 10).

The natural frequency (ω_n) of the system under sinewave excitation exhibits a different trend than that of

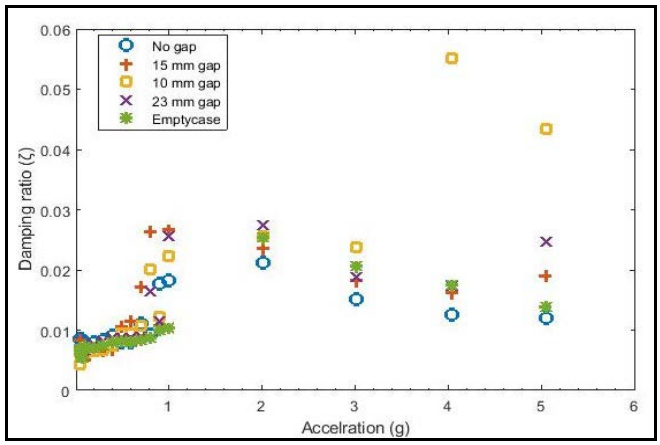

Fig. (9) The effect of acceleration g (peak) on the different gaps of an impact damper's damping ratio (ζ) under sinewave excitation

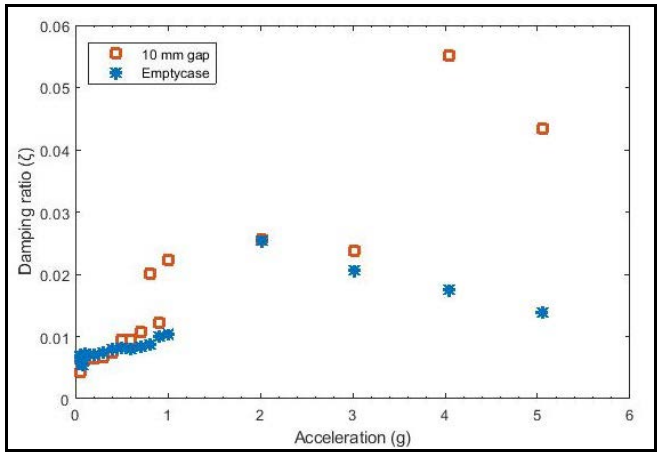

Fig. (10) Comparison of the acceleration g (peak) effect on the damping ratio (ζ) of an impact damper (with 10mm gap) to that of an empty-case under sinewave excitation

the random excitation in that the natural frequency of the 10mm gap is lower than the damper with no gap (Fig. 11). And it is much lower than the empty-case's natural frequency as shown in figure 3.11.

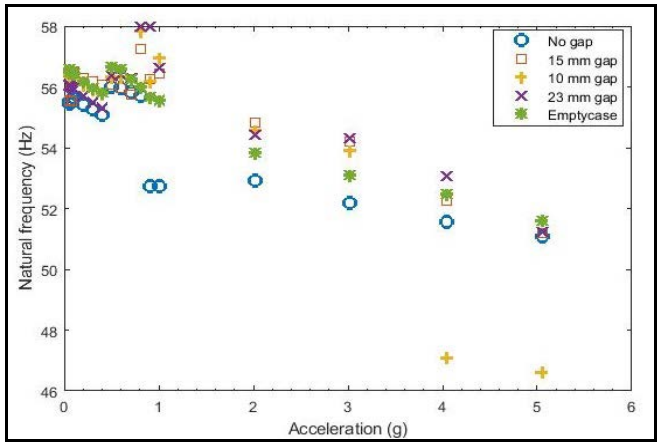

Fig. (11) The effect of acceleration g (peak) on the different gaps of an impact damper's natural frequency (ω_n) under sinewave excitation

DISSIPATED ENERGY IN THE SYSTEM

If a vibrating system is connected to a damper, then due to damping, the amplitude will reduce in each cycle. This is because it is the rule of damping to reduce the amplitude and since the amplitude is reduced in each cycle, it means that energy of the system is dissipated. Thus, the damping in this system is reducing the amplitude by absorbing some energy of the vibrating system, so the dissipated energy of the system under sinewave excitation with gap 10 mm and amplitude 5g is determined by the equation (Appendix C):

$$W = \pi\, c\, \omega\, X^2$$

Stiffness and damping for impact damper:

$$\omega_n = 2\pi f$$

$$= 2\ (3.1415)\ (46.62)$$

$$= 292.91\ rad/s$$

Accounting for the background damping of the test rig:

$$\zeta_{(actual)} = \zeta_{measured} - \zeta_{\ test\ rig}$$

$$= 0.04333 - 0.01382 = 0.02951$$

$$c = 2\zeta m \omega_n$$

$$= 2\ (0.02951)\ (0.6778)\ (292.91)$$

$$= 11.72\ Ns/m$$

Calculating the amplitude's value, $A = X\omega_n^2$

$$X = \frac{A}{\omega_n^2}$$

$$= 49.05 / (292.91)^2$$

$$= 5.7 \times 10^{-4}\ m$$

Dissipated energy (W):

$$W = \pi\, c\, \omega\, X^2$$

$$= (3.1415)\ (11.72)\ (292.91)\ (5.7 \times 10^{-4})^2$$

$$= 3.5 \times 10^{-3}\ J$$

Kinetic energy (T):

$$T = {}^1\!/_2\ m_p\ (\omega X)^2$$

$$= ½\ (11.5)\ [(292.91)\ (5.7 \times 10^{-4})]^2$$

$$= 1.6 \times 10^{-4}\ \ J$$

Calculation of W/T ratio from impact damper:

The Specific damping capacity (ψ) = W/T is calculated from excitation amplitude 0.1 to 5 g as in Table 2.

Table 2: Ratio of dissipated energy per cycle (W) to kinetic energy per cycle (T)

Amplitude (X) m	Kinetic energy per cycle (T) J	Dissipated energy per cycle (W) J	W/T
7.9×10^{-5}	4.5×10^{-8}	3.1e-8	0.7
1.6×10^{-5}	1.8×10^{-7}	7.0e-8	0.4
2.4×10^{-5}	4.1×10^{-7}	2.4e-7	0.6
1.3×10^{-5}	1.2×10^{-7}	5.8e-8	0.5
3.3×10^{-5}	7.8×10^{-7}	7.9e-7	1.0
4.7×10^{-5}	1.5×10^{-6}	1.8e-6	1.2
5.5×10^{-5}	2.2×10^{-6}	3.6e-6	1.6
6.0×10^{-5}	2.7×10^{-6}	2.3e-5	8.5
7.1×10^{-5}	3.6×10^{-6}	5.9e-6	1.6
7.7×10^{-5}	4.4×10^{-6}	3.8e-5	8.6
1.7×10^{-4}	2.0×10^{-5}	4.7e-6	0.2
$2.6\ \chi\ 10^{-4}$	4.5×10^{-5}	1.0e-4	2.2
4.5×10^{-4}	1.0×10^{-4}	2.8e-3	28
5.7×10^{-4}	1.6×10^{-4}	3.5e-3	6.1

One of the simplest ways to model a single particle impact damper is to use a SDOF model in which the particle is represented by mass that can move between rigid walls, which themselves are subject to prescribed motion. The contact between the particle and the walls of the casing can be represented by springs and dampers as shown in figure 12.

The variables x_c and x_p represent the positions of one of the walls and the particle relative to an arbitrary fixed point in space. The second wall remains a fixed distance L from the first one. When the casing walls move with a prescribed time history, useful outputs of the model are the resulting motion of the particle and the force required to maintain the motion of the casing.

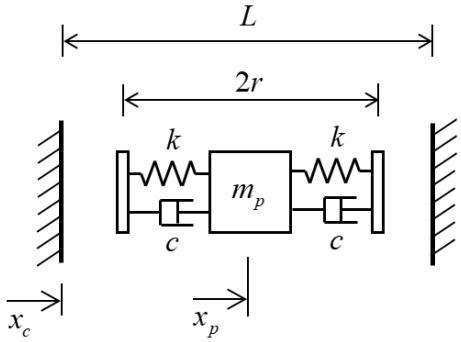

Fig. (12). An SDOF model showing contact between the particle and the casing

Motion of the particle is related to force applied to it using Newton's Second Law,

$$m_p \ddot{x}_p = f$$

It can be seen from the figure that particle-wall contact is not constant and hence the force depends on the contact conditions. No force is transmitted when the particle is not touching a wall. In the absence of body forces such as gravity loading, $f = 0$.

When in contact, force is generated by spring and damper units. However, even when in contact, the spring and damper together cannot exert a tensile force. These conditions are summarised in Table 3.

Time domain simulation

The equation of motion can be solved numerically in Matlab using the function ode45. This function provides a numerical solution to a first order differential equation of the form,

$$\dot{y} = Ay + F,$$

For the impact damper problem this can be achieved by setting

$$y = \begin{bmatrix} x_p \\ \dot{x}_p \end{bmatrix} \quad \text{and,} \quad A = \begin{bmatrix} 0 & 1 \\ -\frac{k}{m_p} & -\frac{c}{m_p} \end{bmatrix}$$

Table (3): Conditions of particle contacts

	Contact with the cylinder bottom	**Contact with the cylinder top**
Condition	$x_c \geq x_p - r$	$x_c \leq x_p + r - L$
Force *f*	$f = f_{spring} + f_{damper}$ $f_{spring} = -k\left(x_p - r - x_c\right)$ $f_{damper} = -c\left(\dot{x}_p - \dot{x}_c\right)$	$f = f_{spring} + f_{damper}$ $f_{spring} = -k\left(x_p + r - x_c - L\right)$ $f_{damper} = -c\left(\dot{x}_p - \dot{x}_c\right)$
No tension	$f > 0$	$f < 0$

In this example, excitation is in the form of prescribed harmonic motion of the casing and the forcing vector depends on the contact,

Contact with the cylinder bottom:

$$\boldsymbol{F} = \begin{bmatrix} 0 \\ \frac{k}{m_p}(x_c + r) + \frac{c}{m_p}\dot{x}_c \end{bmatrix}$$

Contact with the cylinder top:

$$\boldsymbol{F} = \begin{bmatrix} 0 \\ \frac{k}{m_p}(x_c + L - r) + \frac{c}{m_p}\dot{x}_c \end{bmatrix}$$

If the motion of the casing is sinusoidal,

$$x_c = X_c \sin(\omega t)$$
$$\dot{x}_c = \omega X_c \cos(\omega t)$$

The Matlab expression for running the time domain solution has the following form,

[t,y] = ode45('calc',t,y_0);

where t is an array containing the discrete points in time that the solution y is obtained at and y_0 are the starting values. The term 'calc' refers to a function "calc.m" that specifies the differential equation and provides the output $\dot{y}$ (written y_d) for a given input (y) at a particular time (t).

y_d = calc(t,y)

For this particular example, it is convenient to note that,

$$\dot{y}(1) = \dot{x}_p = y(2)$$

and,

$$\dot{y}(2) = \ddot{x}_p = \frac{f}{m_p}$$

where the force *f* depends on the contact conditions defined on the previous page.

This entire example has been coded into the function sdof_impact_damper. Because of the limitation on allowed input and output variables in "calc.m" this function has to encode internal computations to allow the force to be specified. To allow convenient adjustment of the values of variables, the main function sdof_impact_damper rewrites "calc.m" each time it is run.

simulation and comparison to experimental results

In this section, the mathematical model is verified and used to perform the simulation with damping and stiffness parameters obtained from the drop-bounce experiment and system parameters with the vibration amplitude (defined as beam displacement X_c) matching the peak vibration in the experimental tests (Table 4, Fig. 13).

Table (4): Parameters used in the simulation

Particle and system parameters	
Particle mass m	11.5 x 10^{-3} m
Particle radius	12.5 x 10^{-3} m
Stiffness k	40.76 x 10^{3} N/m
Damping c	0.7 Ns/m
Casing length L	40 x 10^{-3} m
Excitation frequency whz	46.62 Hz
Amplitude Xc	5.7 x 10^{-4} m

The specific damping capacity (ψ) W/T per cycle of the simulation is calculated and compared to that of the impact damper experiment (Table 5). There is a small discrepancy between the simulation and experimental results (Fig. 14).

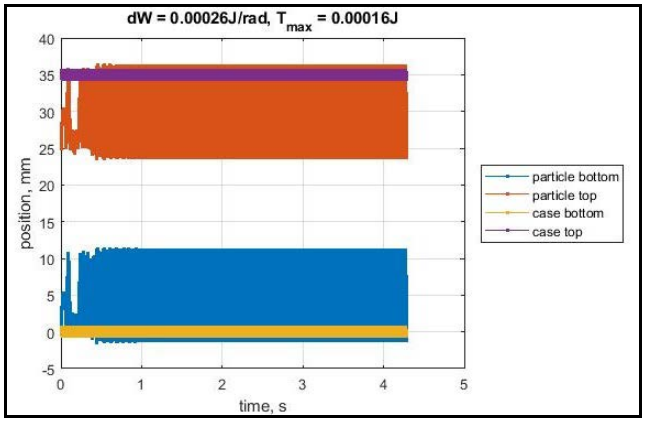

Fig. (13). simulation showing the dissipated energy by radian resulting from a viscoelastic sphere contact with the damper's casing at vibration amplitude (Xc) 5.7 x 10^{-4} m and excitation frequency 46.62 Hz

CONCLUSION

The practical and inert vibration control technology of particle damping is developing considerably at the present stage with ongoing research into its many factors. This study aims to explore the role of contact pressure of the particles and the configuration of its container.

Table 5: Comparing the specific damping capacity (W/T) of experiment and simulation

Amplitude (X) m	W/T simulation	W/T experiment
7.9 X 10^{-6}	0	0.3
4.7 X 10^{-6}	0	1.9
5.5 X 10^{-6}	0	0.5
6.3 X 10^{-6}	0	0.5
7.0 X 10^{-6}	0	0.5
7.9 X 10^{-6}	0	0.7
1.6 X 10^{-5}	0	0.4
2.4 X 10^{-5}	0	0.6
1.3 X 10^{-5}	0	0.5
3.3 X 10^{-5}	0	1
4.7 X 10^{-5}	0.7	1.2
5.5 X 10^{-5}	1.9	1.6
7.1 X 10^{-5}	1.2	1.6
1.7 X 10^{-4}	1.2	0.2
2.6 X 10^{-4}	3.8	2.2

The identification of the main challenge: granular damper properties strongly affected by the extent to which

particles are forced together to form temporary agglomerations such as what is seen in the "bouncing bed" phase. The ability to form and adjust the nature of these agglomerations gives control over the damper effectiveness, so this research focuses on physical ways of controlling this.

The discrepancy between the simulation and experimental results could be caused by the level of uncertainty in the damping ratio data which is showing in the quality of the circle-fit which artificially effect the damping. This uncertainty could be also caused by the nonlinearity

of the system or could be an issue with the shaker drop-out causing more vibrations. Thus, measurements of natural frequency data have a higher level of certainty than the damping ratio data. Considering the uncertainty in the experiment the comparison result is a reasonable outcome.

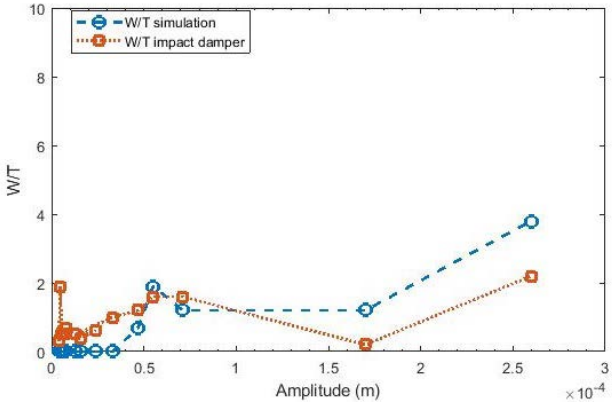

Fig. (14). Comparing the specific damping capacity (W/T) of experiment and simulation

The flexible packet is one way to adjust the agglomerations in a controllable manner. Thus, future work

will concentrate on the design and experiment of a flexible packet damper that can be used to adjust the particle-to- particle contact pressure (and therefore the performance) of a granular damper. The flexible packet comprises a collection of particles that are squeezed together by an elastic membrane which provides a nominal static pressure that is defined by the tension in the membrane. The membrane can be constructed from different materials, but initial work will involve an elastomer for simplicity.

REFERENCES

[1] S. Masri and A. Ibrahim, “Response of the impact damper to stationary random excitation,” *J. Acoust. Soc. Am.*, vol. 53, no. 1, pp. 200-211, 1973.

[2] R. Ibrahim, Vibro-Impact Dynamics, Modelling, Mapping and Applications, Berlin: Springer-Verlag Berlin Heidelberg , 2009.

[3] C. Saluena, T. Pschel and S. Esipov, “Dissipative properties of vibrated granular materials,” *Phys. Rev. E*, vol. 59, no. 4, pp. 4422-44, 1999.

[4] M. Sanchez, C. Carlevaro and L. Pugnaloni, “Effect of particle shape and fragmentation on the response of particle dampers,” *J. Vib. Control* , vol. 20, no. 12, pp. 1846-1854, 2014.

[5] A. Oldzki, I. Siwicki and J. Winiewski, “ Impact dampers in application for tube, rod and rope structures,” *Mech. Mach. Theory* , vol. 34, no. 2, pp. 243-253, 1999.

[6] C. Wong, M. Daniel and J. Rongong, “Energy dissipation prediction of particle dampers,” *Journal of Sound and Vibration*, vol. 319, no. 1-2, pp. 91-118, 2009.

[7] P. Avitabile, Modal Testing: A Practitioner’s Guide, Hoboken, NJ: The Society for Exper-

imental Mechanics and John Wiley & Sons Ltd, 2018.

[8] R. D. Blevins, Fourmulas for Natural Frequency and Mode Shape, New York: Van Nostrand Reinhold Co., 1979.

[9] Z. Lu, Z. Wang, S. Masri and X. Lu, "Particle impact dampers: past, present, and future," *Struct. Control Health Monit.* , vol. 25, no. 1, p. e2058, 2017.

[10] G. Michon, A. Almajid and G. Aridon, "Soft hollow particle damping identification in honeycomb structures," *J. Sound Vib.*, vol. 332, no. 3, pp. 536-544, 2013.

[11] Z. Xia, X. Liu, Y. Shan and X. Li, "Coupling simulation algorithm of discrete element method and finite element method for particle damper," *J. Low Freq. Noise Vib. Act. Control*, vol. 28, no. 3, pp. 197-204, 2009.

[12] Z. Xu, M. Wang and T. Chen, "Particle damping for passive vibration suppression: numerical modelling and experimental investigation," *J. Sound Vib.*, vol. 279, no. 3, pp. 1097-1120, 2005.

[13] Z. Lu, X. Lu, H. Jiang and S. Masri, "Discrete element method simulation and experimental validation of particle damper system," *Eng. Comput.* , vol. 31, no. 4, pp. 810-823, 2014.

Al-Mukhtar Journal of Engineering Research 07 (1): 43-56, 2023
Doi: https://doi.org/10.54172/mx8n6k70

Research Article

Open Access

Modelling and simulation of flexural behavior for reinforced concrete beams using ANSYS

Mohamed Khalifa Bneni[(1)] and Samir Hasuna Ashour[(2)]

***Corresponding author:** mo.bneni@zu.edu.ly Faculty of Engineering, University of Zawia, Libya.

Second Author: S.ashour@zu.edu.ly, Faculty of Engineering, University of Zawia, Libya .

Received:
17 July 2023

Accepted:
05 December 2023

Publish online:
31 December 2023

Abstract

Over the last twenty years, many investigators are used finite element software, to validate and compare the FE results with their experimental research. This work focused on the development of a numerical model implemented by the ANSYS 2022R2 software, to simulate the flexural behavior of the RC beam. Numerical models are tested under four-point bending. To investigate the influence of reinforcement steel ratio and compressive strength of concrete on the flexural capacity of the model. The results indicated that the Finite Element model was able to predict the flexural behavior of the experimental test beam. Furthermore, the influence of different tensile reinforcement ratios has the most effect on the flexural behaviour of the FE models at maximum loads. While the change in concrete compressive strength has affected the flexural performance of the models. This influence shows slight increases in the first crack load and maximum loads of the models. Furthermore, cracking pattern behaviour at the final stage for numerical models showed a good agreement with experimental cracks behaviour.

Keywords: RC Beams, Finite Element Method, ANSYS, Steel Reinforcement Ratio, Compressive Strength.

INTRODUCTION

Experimental studies of the flexural behavior of reinforced concrete beams comprise the cost of materials, equipment for testing, workers and time. Safety and serviceability evaluation of construction structures requires the development of accurate methods and three-dimensional FE models for their analysis. For example, the numerical and experimental studies are conducted side by side. To compare the numerical and experimental results and collect detailed information using numerical models. Also, the experimental studies are becoming expensive and take a long time. The Finite Element Method (FEM) is commonly used for predicting the behavior of structures, and it is often preferred over experimental studies when investigating the behavior of concrete. Many variables have an impact on the accuracy and convergence of the results such as properties of materials, mesh and convergence criteria. Vasudevan and Kothandaraman [1] present several trial analyses of influencing factors on the flexural behavior of numerical models. As, mechanical properties of concrete, mesh density, points loaded, the influence of shear reinforcement on flexural behavior, and steel reinforcement ratios. The results of their study demonstrate the ANSYS program's ability to simulate mechanical properties in the analysis of reinforced concrete beams. Mazen Musmar [2] referred in his study to the performance of the finite element model of the reinforced concrete beams that are

designed to fail in flexure. The work showed the performance of the FE model of the RC beam from where crack pattern, load-deflection curve, mode of failure and behavior material models are implemented in the FE models. This study targets to explain the effective role of FE structural modelling in simulating the performance of RC structures members.

Another study showed that modelling and simulation of reinforced concrete beams using ANSYS program to understand the effect of percentages of steel reinforcement on flexural behavior as under, balanced and over-reinforced beams implemented by Pawar and Pawar [3]. Pranata et al. [4] studied testing of the studied deep beams was performed by FE modelling using ANSYS program. To obtain useful parameters for modelling RC deep beams in FEM modelling, calibrating tests have to be done out of verification and validation processes. Moulika et al. [5] worked in their study that modelled and analyzed reinforced concrete beams when subjected to two-point loads at one-third span from each support, using the Finite Element Analysis tool, called ANSYS software. The numerical model has dimensions length of 600mm, width of 160 mm and height of 160 mm with main steel reinforcement of 3Φ12 mm and 2Φ8 mm at top reinforcement, also stirrups using Φ8 mm/100 mm. The results showed have more sensitive to mesh size, materials properties and load increments.

Tjitradi et al. [6] studied the conduct of structural members of one-layer reinforced concrete beams under tension, balanced and compressive, consequences of collapsed mechanisms with modelling and simulation using ANSYS Workbench. The outcomes displayed that the reinforced concrete members can be analysed using the ANSYS program with the modified three-dimensional model. The numerical model used simulates Multilinear Kinematic Hardening using the compression stress-strain curves of unconfined concrete. The use of the element SOLID 65 in the modelling of concrete materials can specify outcomes by the nonlinear behaviour of reinforced concrete members. Steel reinforcement is used as an axial bar element by taking the discrete engineering model Spar Link Element (LINK8). The behaviours of RC elements can be determined through the analysis of calculation and FEM that beams with the tensile collapsed condition have a lower flexural capacity and collapse behavior is more ductile. On the other hand, many studies focused on the development of a 3D FE model using ANSYS software to analysis the flexural behavior of the RC beam strengthened, and validate numerical results with the experimental results. These papers presented the applications of nonlinear finite element models in the analysis and predict the behavior of RC beams strengthened with U-jacket, CFRP sheets or rods and NSM FRP rods. The numerical results are compared to experimental results of unstrengthen beams. As well, the comparisons are carried out about of load- deflection behavior at mid-span of beams, the ultimate load at failure and cracks pattern [7-11].

The aims of this research are to:

- Select the suitable element types available in ANSYS 2022 R2 software, such as steel reinforcement, concrete, plates of loading, and steel support plates.
- modelling of a 3D model to simulate the behaviour of simply supported RC beams analysis.
- Validation of the numerical model results of the current study by comparison of the experimental results of a tested beam (reference beam CB) implemented by Sharaky et al. [12].
- Studying the effect of two variables such as tensile reinforcement steel and compressive strength of concrete on the behaviour of the numerical model.

MATERIALS AND METHODS

To model and idealize the RC beams in the ANSYS software some elements must be selected. ANSYS's element library [13] contains a lot of different element types. Each element type has a

unique number and a prefix that identifies the element category. Concrete was modelled using solid element SOLID65 with 3-D 8-node solid elements as shown in Fig. 1 (a). The SOLID 65 element is capable of crushing in compression and cracking in tension. The steel reinforcement was modelled using LINK 180 as shown in Fig. 1(b). Moreover, a 3-D structural solid element 185 was used to model the plates of loading and supports as shown in Fig. 1 (c).

The specimen of study is a simply supported reinforced concrete beam. The full-size specimen was 2600 mm × 160mm × 280mm and the clear length of 2400 mm. While the main steel reinforcement was 2Ø12 mm and the top reinforcement of 2Ø8 mm as shown in Fig. 2. The shear steel reinforcement was 8 mm stirrups with spacing between bars of about 100mm .Table 1. displays the concrete material properties used for current model.

Six models divided into two main groups were subjected to four-point bending. We have selected the four - points test to evaluate of behavior flexural of FE models and

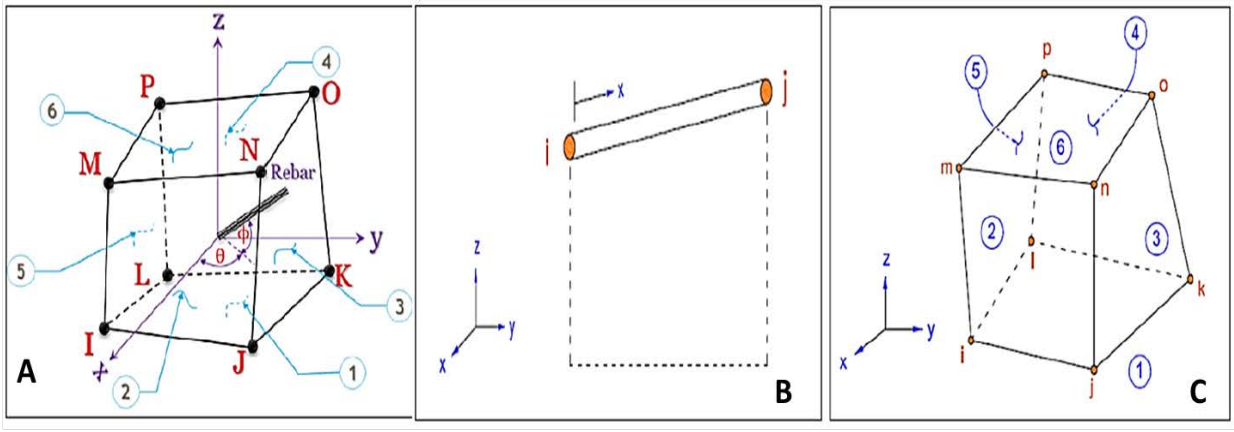

Fig. (1). FE models elements: (a) SOLID65 (b) LINK180 (c) SOLID185[13].

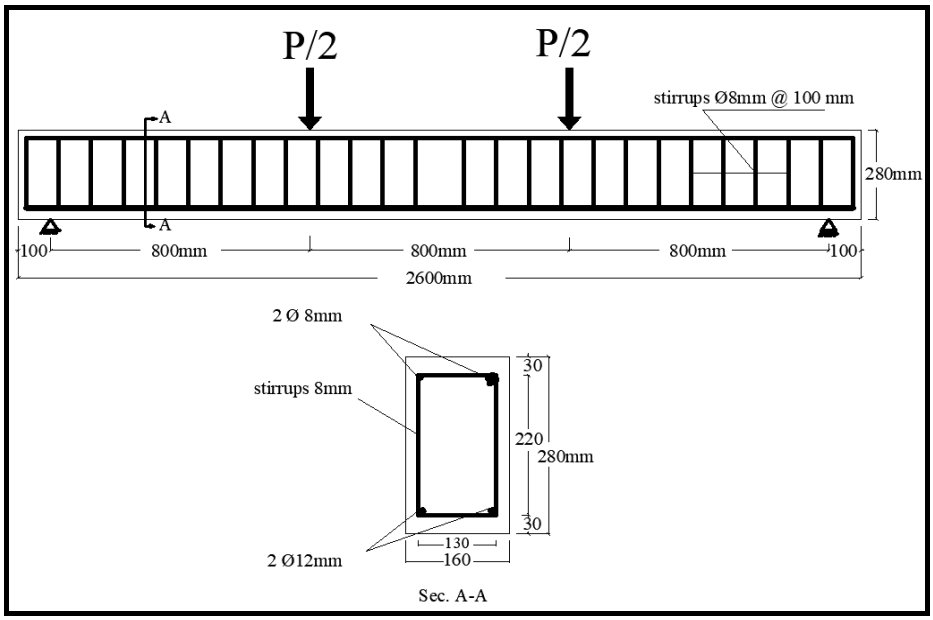

Fig. (2).Tested beam details [12].

Table (1): Concrete material properties used in ANSYS beam model

	Material properties		
		M30	M60
Concrete	Modulus of Elasticity, Ec	25000MPa	36000MPa
	Poisson Ratio, υ	0.2	0.2
	Open Shear Transfer Coef.	0.2	0.2
	Closed Shear Transfer Coef.	0.8	0.8
	Uniaxial Cracking Stress (ft)	2.8 MPa	3.50 MPa
	Uniaxial Crushing Stress (fc)	31 MPa	60 MPa
Tension Reinforcement	Modulus of Elasticity, Es	200 GPa	200 GPa
	Poisson Ratio, υ	0.3	0.3
	Yield stress	545 MPa	545 MPa
	Tangent Modulus	1200 MPa	1200 MPa
Loading & Supporting Plates	Density	7850 kg/m^3	7850 kg/m^3
	Modulus of Elasticity, Es	200 GPa	200 GPa
	Poisson Ratio, υ	0.2	0.2
	Tensile Yield Strength	550 MPa	550 MPa
	Tensile Ultimate Strength	650 MPa	650 MPa

to avoid shear failure. The models were designed as an under-reinforced section, the first group is normal strength concrete, while the second group with high strength concrete. The variable factor for each group in the numerical study using ANSYS software is steel reinforcement ratios. Details of the models for the numerical program are summarized in Table 2

Modelling and Meshing

Modelling of the RC beams is idealized in the ANSYS. The RC beam has been modelled as volumes, such as the concrete, loading plates and supports. While the steel reinforcements and stirrups are modelled as line bodies. The model of RC beam is shown in Fig. 3. Concrete was simulated using a multilinear isotropic hardening model. The stress-strain curve was used to simulate the concrete plasticity based on equations 1 and 2. The concrete material properties are given in Table 1.

Table (2): Numerical models configuration

Type of group	Model ID	Bottom reinforcement	fc	Top reinforcement	Stirrups
Group (A)	B1-Φ12-M30	2-Φ12mm	31MPa	2-Φ8mm	Φ8mm@100mm
	B2-Φ14-M30	2-Φ14mm		2-Φ8mm	
	B3-Φ16-M30	2-Φ16mm		2-Φ8mm	
Group (B)	B4-Φ12-M60	2-Φ12mm	60MPa	2-Φ8mm	
	B5-Φ14-M60	2-Φ14mm		2-Φ8mm	
	B6-Φ16-M60	2-Φ16mm		2-Φ8mm	

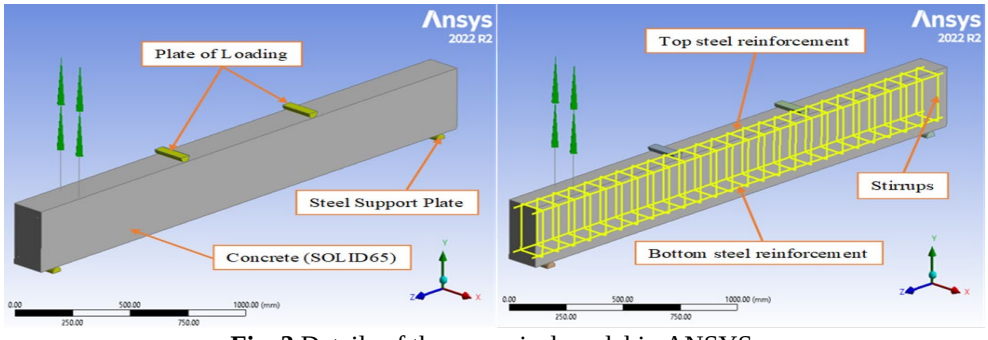

Fig. 3 Details of the numerical model in ANSYS.

$$f = \frac{E_c \varepsilon}{1 + \left(\frac{\varepsilon}{\varepsilon_0}\right)^2} \quad \ldots\ldots\ldots\ldots\ldots\ldots 1$$

$$\varepsilon_0 = \frac{2 f_c^{'}}{E_c} \ldots\ldots\ldots\ldots\ldots\ldots\ldots\ldots 2$$

Where, E_c is Young's modulus for concrete, ε is the concrete strain, and ε_o is the compression failure strain.

Element mesh size sensitivity

On the other hand, sensitivity analysis was done by studying the element's sizes effect of (25*24*16.5) mm, 20mm, 30mm and 40mm, to examine the convergence of the results. Fig. 4 shows the effect of element sizes on the numerical results that were studied and compared to experimental results by Sharaky et al. [12]. The mesh size (25*24*16.5) mm was chosen as it generated good results from the solver keeping the run time at a reasonable length. Fig. 5 presents the mesh size of the numerical model in ANSYS for this study.

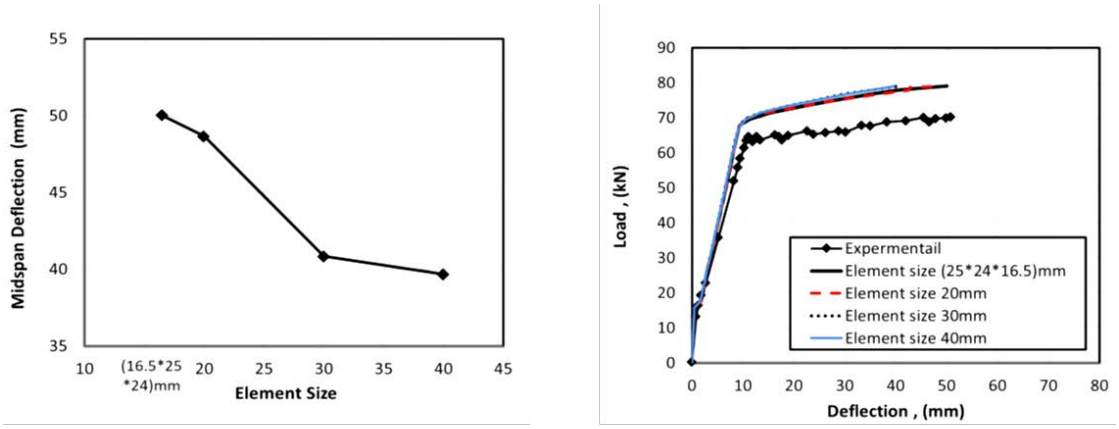

a) Effect of element size on the sensitivity of results

b) Comparison of P-δ curves with different mesh sizes

Fig. (4). Results verification; a) Effect of element size on the sensitivity of results, b) Comparison of P-δ curves with different mesh sizes.

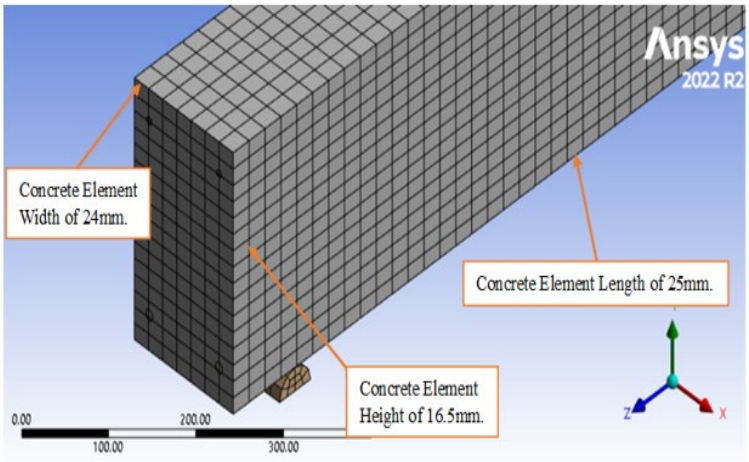

Fig. (5). The meshes of the numerical model in ANSYS

Loading and Boundary Conditions

Displacement boundary conditions are required to constrain the model to obtain a remarkable solution. To confirm that the model works similarly to the testing beam; boundary conditions must be applied to the supports. So, the support conditions in this study will be taken as a pin support with no movement in the X, Y and Z directions. In contrast, another support will be taken as a roller of which there will be only movement in the Z- direction with no movement in the other directions as seen in Fig. 6. The load plate is loaded by applying a remote force on each plate as seen in Fig. 6.

The methodology of this study was done by modelling of geometry body, selecting the type of elements, material properties of concrete and steel, meshing details, finite element analysis, and results as shown in Fig. 7.

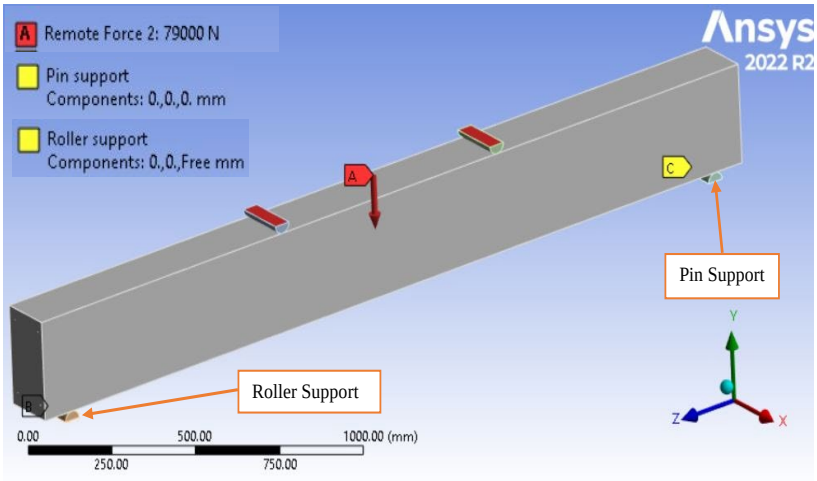

Fig. (6). Loading and boundary conditions of model.

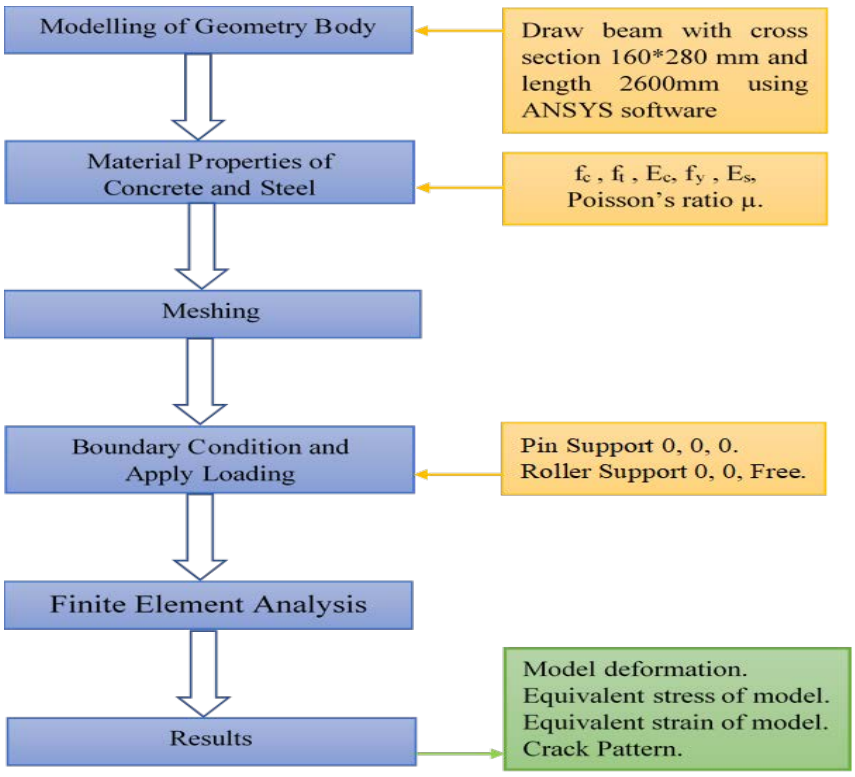

Fig. (7). A flowchart displays the process of the methodology.

RESULTS AND DISCUSSION

Validation of the model

The validation of the FE model must be done to determine the accuracy of the results. The numerical model was simulated and compared to an experimentally tested beam of the study published in the international journal, by Sharaky et al. [12]. Comparing the numerical results to the experimental results, the flexural behavior of the finite element model is acceptable through the load-displacement curve as shown in Fig. 8. The data in the figure clearly shows that the first crack load registered about 15.72kN for the current numerical model compared to 14.7kN for experimental beam [12]. While the yield load, P_y, and mid-span deflection, Δ_y, registered about 67.79kN and 9.43mm for the current numerical model compared to 64.5kN and 11.20mm for the experimental beam, respectively.

On the other hand, Fig. 9. shows the numerical deflection distribution along the model and compares it with that experimentally measured by [12]. It can be noticed that the deflection at the mid-span for the experimental recorded about 1.95mm, 4.12mm, 6.90mm and 9.75mm compared to 2.18mm, 3.62mm, 5.87mm and 8.11mm for deflection of the numerical model with percent difference by (-11.79%), (12.13%), (14.92%) and (16.82%) at loading steps 20kN, 30kN, 45kN, 60kN, respectively. The distribution shows convergent results in the elastic zone as a linear relationship exists and an increase in the percentage difference at the end elastic region and after yield stress of steel, due to the plastic region as seen in Fig.8. Also, there are microcracks in the concrete for the tested beam due to the production of concrete by shrinkage that it is not included in the numerical model and it affects numerical results. Overall, there was an agreement and convergence in the load-deflection behaviour.

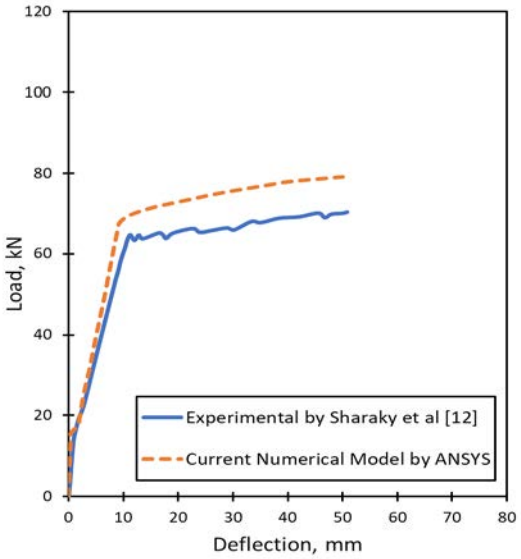

Fig.8 Load-deflection curve of experimental results by [12] and numerical model

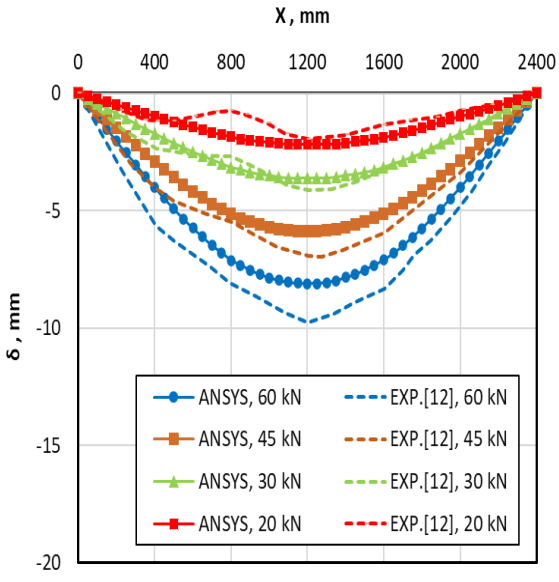

Fig. 9 Details deflection of numerical model compared to experimental results

Parametric study

Table 3. presents the numerical results of finite element models in this research for all specimens using ratios of steel reinforcement and various compressive strengths of concrete. It includes the first crack load, P_{cr}, yield load, P_y, yield deflection, Δ_y, the maximum load, P_u, the maximum deflec-

tion, Δ_u, ductility index, μ, and the failure modes. The numerical models failed due to concrete crushing after yielding the steel reinforcement.

Table (3): Numerical results of the FE Models

Model ID	P_{cr} (kN)	P_y (kN)	Δ_y (mm)	P_u (kN)	Δ_u (mm)	μ	Failure mode
B1-Φ12-M30	15.72	67.79	9.43	79	50.02	5.30	concrete crushing
B2-Φ14-M30	16.13	90.73	10.16	103	41.09	4.04	concrete crushing
B3-Φ16-M30	17.80	119.8	12.18	136	39.13	3.21	concrete crushing
B4-Φ12-M60	16.52	71.22	9.39	83	29.34	3.12	concrete crushing
B5-Φ14-M60	18.87	94.25	9.81	107	32.75	3.33	concrete crushing
B6-Φ16-M60	21.50	123.3	10.86	140	34.54	3.18	concrete crushing

Effect of tensile reinforcement ratios

The effect of the tensile reinforcement ratios on the flexural behavior of the numerical models was investigated in the difference between numerical results and experimental results due to the toughening mechanisms. So, the model was able to predict the experimental outcomes in an acceptable manner. This section. Fig.10 illustrate the effect of tensile reinforcement steel ratios on load-deflection behavior of the numerical models having the normal strength concrete M30 and tensile reinforcement ratios of 0.6%, 0.8% and 1%, which equals the area steels about by 2Φ12mm, 2Φ14mm and 2Φ16mm, respectively. We can notice that the numerical model of B3-Φ16-M30 recorded an ultimate load of 136 kN, while values of 103 kN and 79 kN were recorded for models B2-Φ14-M30 and B1-Φ12-M30 respectively. The increasing percentages are 72.1% and 30.3% for tensile steel ratios using 1% and 0.8% compared to 0.6% respectively.

Fig.11 illustrate the effect of tensile steel reinforcement ratios on load-deflection behavior of the numerical models having the high strength concrete M60 and tensile reinforcement ratios of 0.6%, 0.8% and 1%, which equals the area steels about by 2Φ12mm, 2Φ14mm and 2Φ16mm, respectively. We can notice that the numerical model of B6-Φ16-M60 recorded an ultimate load of 140 kN while values of 107 kN and 83 kN were recorded for models B5-Φ14-M60 and B4-Φ12-M30 respectively. The increasing percentages are 68.6% and 28.9% for tensile steel ratios

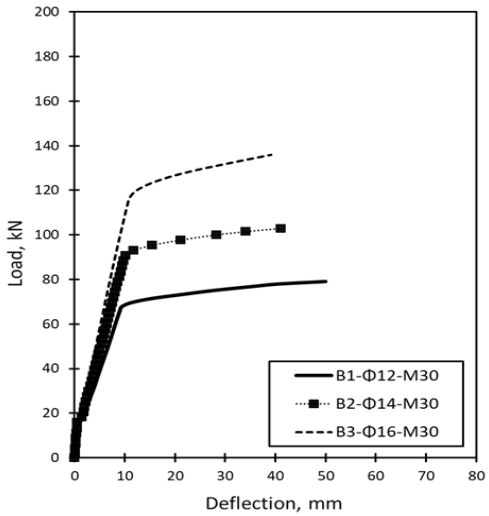

Fig .(10). Load - deflection curves of numerical models with different areas steel for M30

using 1% and 0.8% compared to 0.6% respectively. These results that it confirms the effect of change longitudinal steel reinforcement ratios on the load-deflection curve for the numerical models by ANSYS software. On the other hand, the mid-span deflection of B3-Φ16-M30 model was decreased at the same applied load of other models which means a raise stiffness due to increasing of tensile steel reinforcement ratios. FE model is able to simulate the flexural behaviors of RC beams using a change of tensile steel reinforcement ratios.

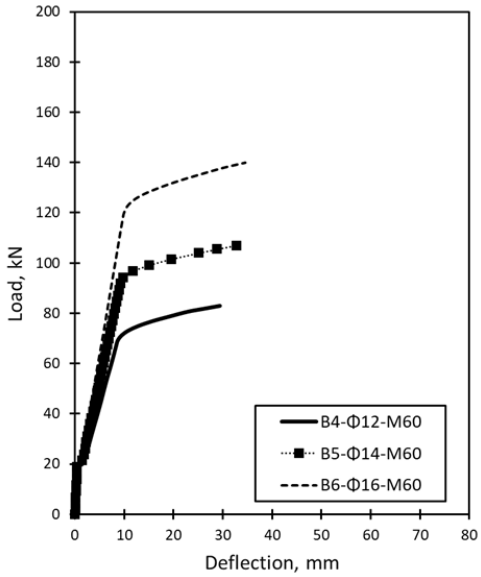

Fig.11 Load - deflection curves of numerical models with different areas steel for M60

Effect of compressive strength of concrete

This section presents, a comparison between the effect of change compressive strength proposed in this work on the flexural behavior of the numerical models. The load-deflection behavior is considered to be an indication of the effect of compressive strength on behavior for the FE models. This analysis aims to determine the efficiency of the model. The effect of the compressive strength on the flexural strength of FE models, with concrete compressive strength of M30, M60 and changing of tensile steel areas are given in Fig. 12.

For tensile reinforcement steel of 2Φ12mm as shown in Fig. 12 (a), models of B1-Φ12-M30 and B4-Φ12-M60 recorded the first cracking load increases from 15.72 kN to 16.52 kN by a percentage enhancement equals 5.0%, respectively. While the value of the ultimate load increases from 79 kN for model B1-Φ12-M30 to 83 kN for model B4-Φ12-M60, the percentage increase is 5.0 %. Moreover, the mid-span deflection at ultimate loads of models is 50.02 mm and 29.34 mm, with percentage decreases of 41.3%, respectively. Fig. 12 (b) presents the behavior of FE models B2-Φ14-M30 and B5-Φ14-M60 with reinforcement steel area of 2Φ14mm. It is observed that the first cracking load increases from 16.13 kN of specimen B2-Φ14-M30 to 18.87 kN of specimen B5-Φ14-M60, by a percentage enhancement equals 17.0%. While the value of the ultimate load increases from 103 kN for model B2-Φ14-M30 to 107 kN for model B5-Φ14-M60, the percentage increase is 5.0 %. Moreover, the mid-span deflection at ultimate loads of models is 41.09 mm and 32.75 mm, with percentage decreases of 20.3%, respectively. Fig. 12 (c) presents the behavior of FE models B3-Φ16-M30 and B6-Φ16-M60 with reinforcement steel area of 2Φ16mm. It is observed that the first cracking load increases from 17.80 kN of specimen B3-Φ16-M30 to 21.5 kN of specimen B6-Φ16-M60, by a percentage enhancement equals 20.7%. While the value of the ultimate load increases from 136 kN for model B2-Φ14-M30 to 140 kN for model B5-Φ14-M60, the

percentage increase is 3 %. Moreover, the mid-span deflection at ultimate loads of models is 39.13 mm and 34.54 mm, with percentage decreases of 11.7%, respectively.

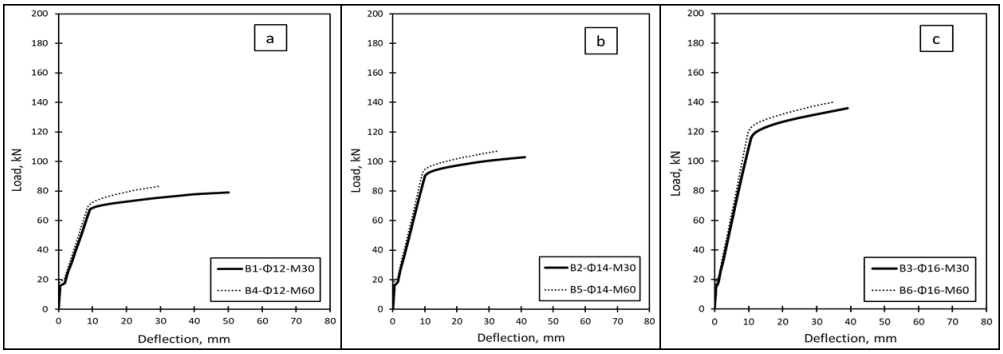

Fig. (12). Load - deflection curve of FE models with change compressive strength

Stress contours and crack pattern of the FE models

The compressive, tensile stress contours and cracks pattern are shown in Figs. 13-18, for numerical models at the ultimate stage loading. As seen in the figures the stress contours of the ANSYS software can effectively display stress prediction and development in the concrete for each mode which depends on various parameters such as change of reinforcing steel ratio and concrete compressive strength. The crack patterns noticed from the finite element analysis at ultimate loads that the FE models using a variety of ratios reinforcement steel failed in flexural by yielding main steel followed by concrete crushing and a high spread of cracks in the mid-span of the models.

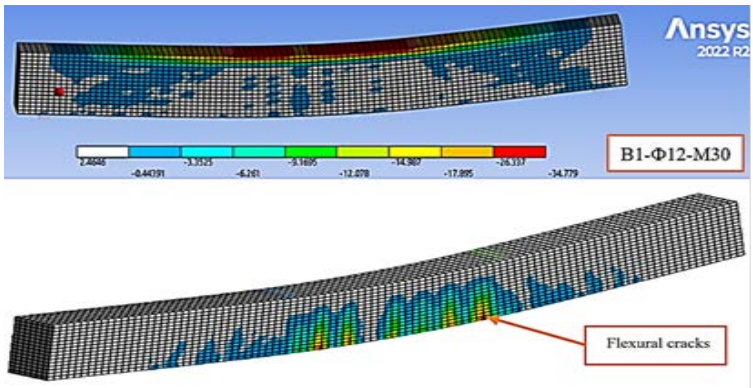

Fig. 13 Numerical stress contours and crack patterns of model B1-Φ12-M30.

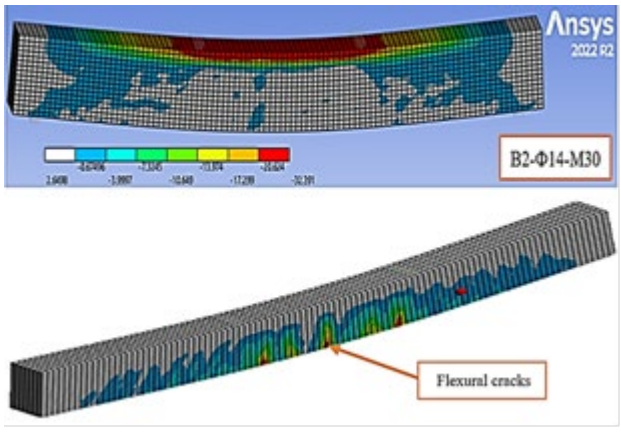

Fig. 14 Numerical stress contours and crack patterns of model B2-Φ14-M30.

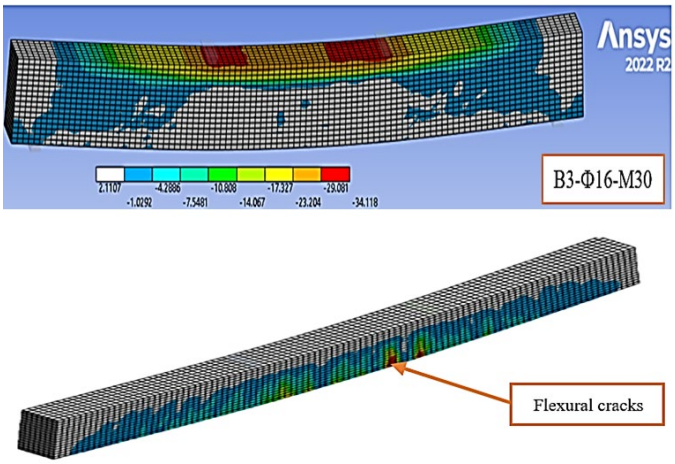

Fig. 15 Numerical stress contours and crack patterns of model B3-Φ16-M30.

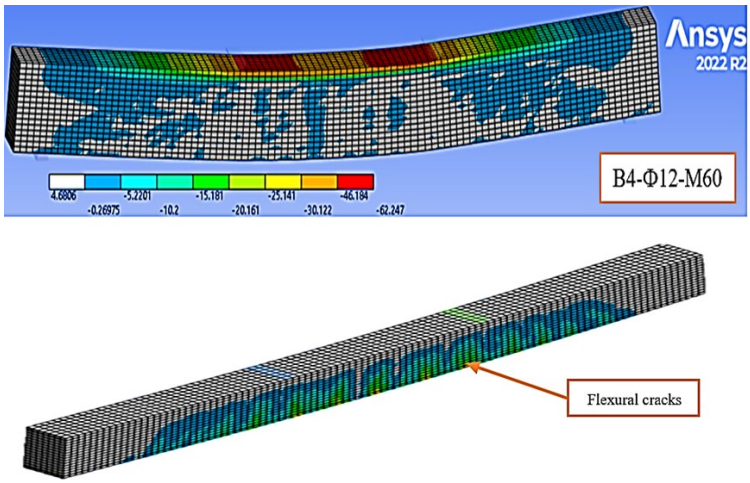

Fig. 16 Numerical stress contours and crack patterns of model B4-Φ12-M60

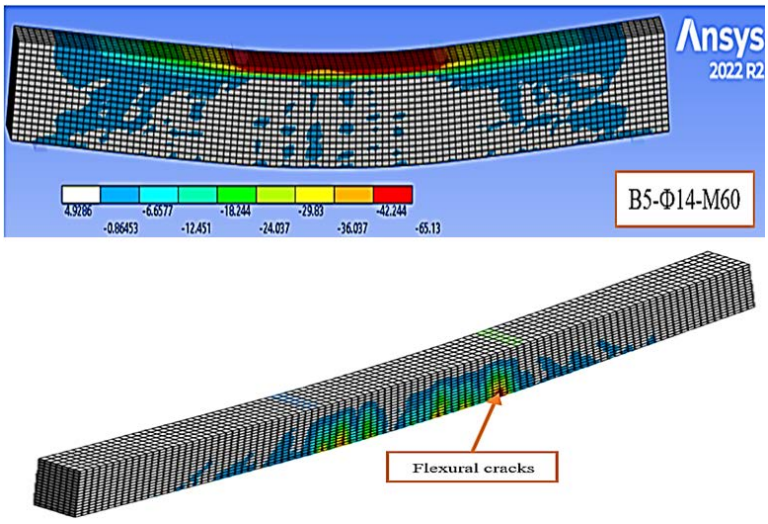

Fig. 17 Numerical stress contours and crack patterns of model B5-Φ14-M60

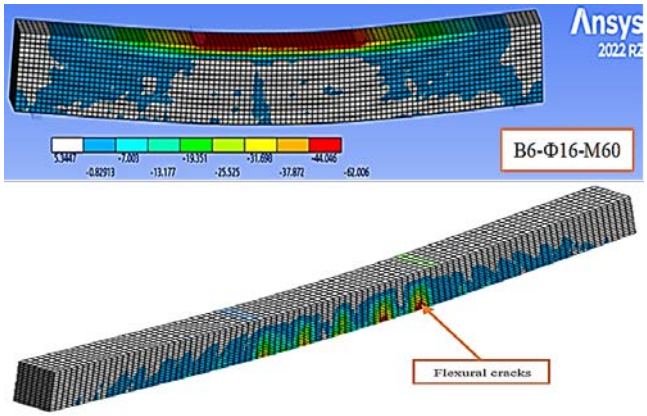

Fig. 18 Numerical stress contours and crack patterns of model B6-Φ16-M60

Stresses in main steel bars

The axial tensile stresses in steel rebars were mapped from FE models as shown in Fig. 19. It can be seen that the upper contour lines which represent the top steel reinforcement showed negative stress values indicating

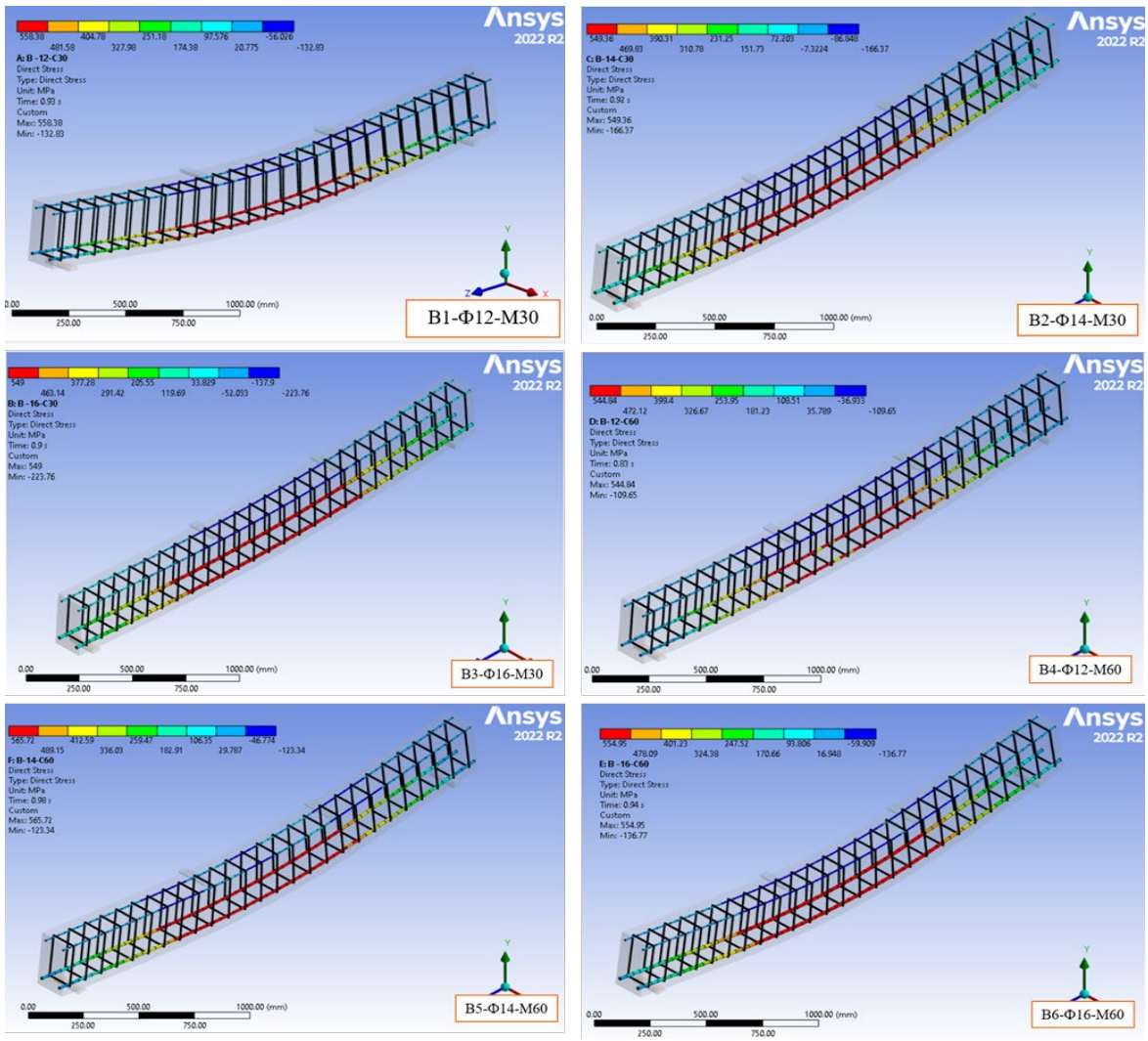

Fig. 19 Stress in the reinforcement steel of FE models at yield point.

compressive stresses while the lowest contour lines which represent the main steel reinforcement showed positive stress values indicating tensile stresses. Moreover, the stresses in the steel reinforcement of all models reached the yield strength.

CONCLUSIONS

The The numerical study allows us to conclude the following:

- The current numerical model was developed using ANSYS 2022 R2 software that was able to predict and simulate of the flexural behavior of reinforced concrete beam tested.
- According to the results, increasing the tensile steel reinforcement ratios has a considerable effect on the load-deflection capacity for the FE models.
- It was concluded that increasing the concrete compressive strength was found to remarkably affect the load-deflection behaviour of the numerical models. Furthermore, it has slightly affected the structural stiffness of the numerical models.
- The cracking pattern of the FE models in ANSYS, compatible with experimental manners.

REFERENCES

[1] Vasudevan, G. and Kothandaraman, S., "Parametric study on Nonlinear Finite Element Analysis on flexural behaviour of RC beams using ANSYS", International Journal of Civil and Structural Engineering, Vol. 2, No. 1, pp. 98 – 111, 2011.

[2] Musmar, M., "Nonlinear Finite Element Flexural Analysis of RC Beams", International Journal of Applied Engineering Research, Vol. 13, No. 4, pp. 2014 – 2020, 2018.

[3] Pawar, V. S. and Pawar, P. M., "Modelling of Flexural Failure in Reinforced Concrete Beams as Under, Balanced and Over-reinforced", International Journal of Engineering Trends and Technology, Vol. 36, No. 8, pp. 394 – 400, 2016.

[4] Pranata, A. Y., Tjitradi, D. and Prasetia, Horizontal I., "Web Reinforcement Configuration Analysis of Deep Beam Capacity and Behavior using Finite Element Model in, Engineering", Technology & Applied Science Research, Vol. 10, No. 1, pp. 5242 – 5246, 2020.

[5] Diyyala Naga Moulika, Reshma Vasireddy and P. Polu Raju "Modelling and Analysis of Reinforced Concrete Beam under Flexure using ANSYS", International Journal of Civil Engineering and Technology, Vol. 8, No. 3, pp. 1103 – 1111, 2017.

[6] Tjitradi, D., Eliatun, E. and Taufik, S., "3D ANSYS Numerical Modeling of Reinforced Concrete Beam Behavior under Different Collapsed Mechanisms", International Journal of Mechanics and Applications, Vol. 7, No. 1, pp. 14 – 23, 2017.

[7] Majeed, S. A., "Finite Element Analysis of Strengthened Reinforced Concrete Beams", Al-Rafidain Engineering Journal, Vol. 21, No. 1, pp. 134 – 145, 2011.

[8] Al-Jurmaa M. A., "Non-Liner Three Dimensional Finite Elements Analyses of Reinforced Concrete Beams Strengthened by CFRP", The Iraqi Journal for Mechanical and Material Engineering, Special Issue (D), pp. 62 – 71.

[9] Martin, A. M. and Kuriakose, M., “Finite Element Modeling and Analysis of Reinforced Concrete Beam Retrofitted with Fibre Reinforced Polymer Composite”, International Journal of Engineering Trends and Technology, Vol. 38, No. 4, pp. 190 – 197, 2016.

[10] Ortes, F., Sayin, B., Bozkurt, T. S. and Akcay, C., “Numerical Simulation of Structural Behavior of NSM CFRP Strengthened RC Beams Using Finite Element Analysis”, The 12th International Symposium on Fiber Reinforced Polymers for Reinforced Concrete Structures (FRPRCS-12) & The 5th Asia-Pacific Conference on Fiber Reinforced Polymers in Structures (APFIS-2015) Joint Conference, Nanjing, China, 2015.

[11] Sharaky, I.A., Reda, R.M., Ghanem, M., Seleem, M.H., and Sallam, H.E.M., “Experimental and numerical study of RC beams strengthened with bottom and side NSM GFRP bars having different end conditions”, Construction and Building Materials, Vol. 149, pp. 882-903,2017.

[12] Sharaky, I.A., Torres, L., Comas, J. and Barris, C., “Flexural response of reinforced concrete (RC) beams strengthened with near surface mounted (NSM) fibre reinforced polymer (FRP) bars”, Composite Structures, Vol. 109, pp. 8 – 22, 2014.

[13] ANSYS, “Release 2022/R2 Documentation”, ANSYS Inc.,2022, http://www.ansys.com.